Supplementary Information

S-1 Experimental section

S-1 Experimental section

S-1.1. Substrate, precursor and electrolytes preparation

1. Bare Ni foam (NF) substrate: A porous NF (1×1 cm^2) was used as the substrate to support the deposition of conductive materials to fabricate the WCuBP micro-leaf cluster (MLC). The NF was sonicated in 6 M hydrochloric acid (HCl) for 20 min to remove surface contaminants, followed by an additional 20 min sonication in DI water to eliminate acid residues and remaining chemicals. The characterization of bare NF is shown in Figure S1.

2. Precursor preparation*:* The WCuBP precursor was prepared by dissolving copper(II) sulfate ($CuSO_4$, ACS, ≥ 98.0%), boric acid (H_3BO_3, ACS, ≥ 99.5%), sodium hypophosphite monohydrate ($NaH_2PO_2.H_2O$, ACS, ≥ 99.0%), sodium tungstate dihydrate ($Na_2WO_4 \cdot 2H_2O$, ACS, ≥ 99.0%), urea (CH_4N_2O, ACS, ≥ 99.0%) and ammonium fluoride (NH_4F, ACS, ≥ 98.0%) in 30 ml of DI water. The molarity of each chemical is provided in the corresponding section. All chemicals purchased from Sigma-Aldrich, USA, were used as received without further purification.

3. Electrolyte preparation: Potassium hydroxide (KOH, pH ~ 14), sulfuric acid (H_2SO_4, pH ~ 0) and phosphate buffered saline (PBS, pH ~ 7.4) were dissolved in 30 ml DI water to prepare alkaline, acidic and neutral electrolytes. The seawater was collected from the Yellow Sea (Incheon, South Korea) and the river water was collected from the Han River (Seoul, South Korea).

S-1.2. Fabrication of WCuBP micro-leaf cluster (MLCs) electrode

WCuBP MLC electrode was fabricated using a single-step hydrothermal method. The precursor solution containing 1.2 mM $Na_2WO_4 \cdot 2H_2O$, 3 mM $CuSO_4$, 3.6 mM H_3BO_3, 8.4 mM $NaH_2PO_2 \cdot H_2O$, 18 mM CH_4N_2O and 2 mM NH_4F in 30 ml DI water was used to synthesize the optimal WCuBP electrode for electrochemical water splitting. The concentrations of Cu, B and P were adopted from our previous work on the CuBP electrocatalyst [1]. W was newly incorporated to synthesize the WCuBP electrocatalyst and evaluate its contribution to catalytic performance. The prepared precursor was

magnetically stirred for 10 min to obtain a homogeneous solution. Next, the solution was poured into a Teflon-lined stainless-steel autoclave with a piece of cleaned Ni foam. The hydrothermal reaction was placed in an oven at 160 ^{o}C for 4 hrs. After the reaction, the electrode was taken out and vacuum annealed at 50 °C for 30 min to improve the surface crystallinity. The formation of the WCuBP electrode can be explained as follows ~

$$Na_2WO_4{\cdot}2H_2O + CuSO_4 + H_3BO_3 + NaH_2PO_2.H_2O + CH_4N_2O + NH_4F + n.H_2O \quad (1)$$

Precursor ionization process

$$Na_2WO_4{\cdot}2H_2O \rightarrow W^{2+} + 2Na^{2+} + OH^- + 2H_2O \quad (1\text{-}1)$$

$$CuSO_4 \rightarrow Cu^{2+} + SO_4^{2-} \quad (1\text{-}2)$$

$$H_3BO_3 \rightarrow B(OH)_3 \rightarrow B^{3+} + 3OH^- \quad (1\text{-}3)$$

$$NaH_2PO_2.H_2O \rightarrow PH_3 + Na_2HPO_4 + 2H_2O \rightarrow P^{3-} + 3H^+ + 2Na^+ + HPO_4^{2-} + 2H_2O \quad (1\text{-}4)$$

$$CH_4N_2O + 2H_2O \rightarrow CO_2 \uparrow + 2NH_3 \quad (1\text{-}5.1)$$

$$2NH_3 + 2H_2O \rightarrow 2NH_4^+ + 2OH^- \quad (1\text{-}5.2)$$

$$NH_4F \rightarrow NH_4^+ + F^- \quad (1\text{-}6)$$

$$\rightarrow WCuBP + 3Na^+ + HPO_4^{2-} + SO_4^{2+} + 3NH_4^+ + F^- + 4H_2O \quad (2)$$

The hydrothermal fabrication of the WCuBP electrode involves multiple chemical reactions under controlled high pressure and temperature. The ionization process of each chemical is detailed in Eqs. 1-1 – 1-6. Specifically, the $Na_2WO_4{\cdot}2H_2O$ underwent a decomposition process to form W^{2+} ions, serving as the source of the W element. Further, $CuSO_4$ dissociates into Cu^{2+} and SO_4^{2-} ions while H_3BO_3 decomposes into B^{3+} and OH^- ions. $H_2NaPO_2{\cdot}H_2O$ breaks down to PH_3 and disodium hydrogen phosphate (Na_2HPO_4) as shown in Eq. (1-4). PH_3 and Na_2HPO_4 went through a further dissolution, releasing P^{3-}, H^+, Na^+ and HPO_4^{2-} ions into the solution. Urea functions as a growth-controlling agent

that can modify nucleation rate and form NH_4^+ ions, which helps to increase hydrogen bonding between the metallic and non-metallic precursors [2,3]. NH_4F also acts as a coordinating agent, which can help to stabilize metal ions in the solution [4]. This coordination can influence the nucleation and growth of the materials along with the pH of the solution.

S-1.3. Synthesis of reference Pt/C and RuO_2 electrodes

1.Pt/C electrode: The HER benchmark electrode Pt/C was synthesized using a soaking method. 20 mg of Pt/C powder and 60 µL of 5 wt% of Nafion (117 solutions, Sigma-Aldrich) were dispersed in a mixture of ethanol (5 ml) and DI water (5 ml). The mixture was then ultrasonicated for 30 min to ensure uniform dispersion. A cleaned Ni foam was dipped into the solution for 30 min to fabricate the Pt/C electrode. Here, Nafion acts as a binder to deposit Pt/C on the porous NF, which functions as a conductive substrate for the electrocatalytic reaction [5]. The surface morphological, elemental composition and electrochemical characterization of the HER benchmark Pt/C can be seen in Figure S3.

2. RuO_2 electrode: Similarly, the OER benchmark electrode RuO_2 was fabricated using the same soaking approach. The precursor was prepared by dispersing 40 mg of RuO_2 powder and 60 µL of 5 wt% Nafion into an ethanol and DI water mixture and sonicated for 30 min. Then, the cleaned NF substrate was immersed for 30 min to prepare the RuO_2 electrode. The characterization for the OER benchmark RuO_2 is provided in Figure S4.

S-1.4. Morphological and Optical Characterization

The morphological and elemental composition of WCuBP MLCs electrodes was examined using a scanning electron microscope (SEM, COXEM CX-200, South Korea) and energy-dispersive x-ray spectroscopy (EDS, Noran System 7, Thermo Fisher, USA). The Raman spectrum was obtained by using a NOST system (Nostoptiks, Gyeonggi-do, Korea) equipped with a 532 nm laser, spectrograph

(ANDOR sr-500) and charge-coupled device (CCD). X-ray diffraction (XRD, D8 Advance, Bruker, USA) pattern was used to analyze the crystalline phase at a scanning rate of 2º /min by the Cu Kα radiation (λ = 1.5406 Å). To understand the crystal phase and structure of the WCuBP electrode, a transmission electron microscope (TEM, JEM-2100F, JEOL, Japan) was used. X-ray photoelectron spectroscopy (XPS, FC-XP10, Thermo Fisher Scientific, USA) was utilized to understand the chemical state and elemental composition of WCuBP at 1.5 KV under < 10−8 torr with the X-ray spot size of 10 μm.

S-1.5. Electrochemical Characterization

The electrochemical performance was evaluated by using an electrochemical workstation (Wizmac, South Korea) with standard three-electrode (3-E) and two-electrode (2-E) configurations in 1 M KOH. In the 3-E system, WCuBP, graphite rod and Ag/AgCl were used as the working electrode (WE), counter electrode (CE) and reference electrode (RE), respectively. The potential (E) conversion for reversible hydrogen electrode (RHE) was based on the following equation: E [V vs RHE] = E(Ag/AgCl) + 0.197 + 0.059 × pH. Linear sweep voltammetry (LSV) was performed at a scan rate of 5 mV/s to obtain polarization curves. Electrochemical measurements were conducted within the potential range between - 0.6 V and 0.2 V versus RHE for the HER and 1.2 and 2.2 V versus RHE for the OER. All the electrochemical measurements were plotted as received, without iR compensation.

The optimal scan rate for HER and OER LSV measurements was determined to be 5 mV/s through a comparative study of different scan rates (2, 5, 8 and 10 mV/s), as shown in Figure S5. A higher scan rate decreases the diffusion layer, as described by the Randles-Sevcik equation: Current response, i_{mp} (A) = $0.446nFAL^{o}(nF\upsilon D_{o}/RT)^{1/2}$ [6]. Where n is the number of electrons transferred in the redox reaction, A (cm^2) is the electron-treated active surface, F is the faradaic constant (C mol^{-1}), D_o (cm^2 s^{-1}) is the diffusion coefficient of the oxidized analyte, C_o (mol cm^{-3}) is the concentration of the analyte, R ($JK^{-1}mol^{-1}$) is the gas constant and T (K) is the temperature. For a

diffusion-controlled and electrochemically reversible electron transfer process, the Randles-Sevcik equation describes the linear increase of peak current (i_{mp}) with the square root of the scan rate υ(V/S) [7]. An excessively high scan rate (10 mV/s) decreases the current density due to the limited diffusion layer and reduced effective reaction area. Therefore, the middle range of scan rate 5 mV/s is usually widely adopted throughout the electrochemical measurements [8]. The Tafel slope was determined from the linear portion of the LSV curves using the equation: η = a + b log |j|, where η is the overpotential, a is a constant, b is the Tafel slope and j is the current density.

Electrochemical impedance spectroscopy (EIS) was measured at a fixed current density of 10 mA/cm^2 for both HER and OER within the range of 100 kHz to 0.1 Hz with an amplitude of 5 mV. The EIS measurement near the catalytic turnover region at different voltages is shown in Figure S6. The cyclic voltammetry (CV) was conducted in the non-faradic region between 0.10 V and 0.30 V for HER and between 1.04 V and 1.14 V for OER, at different scan rates from 40 to 80 mV/s. The HER/OER C_{dl} values were obtained by analyzing the slope of the current density difference plots using the equation $J = (J_a - J_c)/2$ [9]. Further, the electrochemical surface area (ECSA) was determined using the equation $ECSA = \frac{C_{dl}}{C_s} \times s_g$, where C_s is the specific capacitance (typically 0.04 mF/cm^2) [10] and S_g is the geometrical surface area (0.25 cm^2, 0.5 × 0.5 cm^2) for WCuBP. The performance of WCuBP was investigated across different pH conditions using 1 M KOH (alkaline), 0.5 M H_2SO_4 (acidic), and 1 M PBS (neutral) electrolytes.

S-1.6. Turnover frequency (TOF) calculations WCuBP electrode

Turnover frequency is the number of reactant molecules converted into the desired product for each catalytic site per unit of time under specific reaction conditions [11]. The hydrogen and oxygen generation by the catalyst can be calculated using the following equations [12].

General TOF equation :

$$\text{TOF} = \frac{\dfrac{Total\ number\ of\ H_2\ or\ O_2\ turnover}{Geometric\ area\ (cm^2)} \times Current\ density}{Number\ of\ active\ sites}$$

The total number of H_2 at turnover:

$$= \left(j\frac{mA}{cm^2}\right)\left(\frac{1\frac{C}{s}}{1000\ mA}\right)\left(\frac{1\ \frac{mol}{e}}{96485\ C}\right)\left(\frac{1\ mol\ H_2}{2\ \frac{mol}{e}}\right)\left(\frac{6.022\ \times\ 10^{23} mol\ H_2}{1\ mol\ H_2}\right)$$

$$= 3.12\ \times\ 10^{15}\left(\frac{H_2/s}{cm^2}\right) per\ \left(\frac{mA}{cm^2}\right)$$

The total number of O_2 at turnover:

$$= \left(j\frac{mA}{cm^2}\right)\left(\frac{1\frac{C}{s}}{1000\ mA}\right)\left(\frac{1\ \frac{mol}{e}}{96485\ C}\right)\left(\frac{1\ mol\ O_2}{4\ \frac{mol}{e}}\right)\left(\frac{6.022\ \times\ 10^{23} mol\ O_2}{1\ mol\ O_2}\right)$$

$$= 1.56\ \times\ 10^{15}\left(\frac{O_2/s}{cm^2}\right) per\ \left(\frac{mA}{cm^2}\right)$$

Metallic active sites of WCuBP

$$= \frac{EDS\ wt\ \%}{100} \times amonut\ of\ loading\ per\ area \times Molecular\ mass \times \left(\frac{Avogadro}{Per\ concentr}\right.$$

$$= \frac{31.35}{100} \times 0.18\frac{mg}{cm^2} \times \frac{1\ mmol}{183.84\ mg}\frac{63.91}{100} \times 0.18\frac{mg}{cm^2} \times \frac{1\ mmol}{63.54\ mg} \times \left(\frac{6.022\ \times\ 10^{23}\ mmol}{2\ mmol}\right)$$

$$= 1.67 \times 10^{17}\ Active\ sites.cm^{-2}\ \text{per mole}$$

The above equation can be used to determine the number of active sites in the optimized WCuBP electrocatalyst. The average weight percentages of W and Cu were 31.35 and 63.91 (wt%), respectively, based on the EDS analysis as shown in Figure S15. W and Cu atoms were considered electrochemically active on the WCuBP catalytic surface and played a role in the HER/OER reactions.

The loading material was 0.18 mg, determined from the weight difference between bare Ni (0.476 g) and the loaded sample (0.656 g). The molar mass of W is 183.84 mg/mmol and Cu is 63.54 mg/mmol, where 1 amu is 1 g/mol.

HER TOF of WCuBP:

$$\text{HER TOF} = \frac{3.12 \times 10^{15} \times 300}{1.67 \times 10^{17}}$$

$$= 5.60 \text{ site}^{-1} \text{ s}^{-1}$$

The HER TOF of WCuBP electrodes can be calculated as above. The 15, 30, 60 and 120 min annealed WCuBP electrodes demonstrated the HER current density of 285.6, 300, 266.7 and 235 mA/cm^2 at fixed 180 mV overpotential in 1 M KOH.

OER TOF of WCuBP:

$$\text{OER TOF} = \frac{1.56 \times 10^{15} \times 300}{1.67 \times 10^{17}}$$

$$= 2.80 \text{ site}^{-1} \text{ s}^{-1}$$

Similarly, the OER TOF of WCuBP electrodes can be calculated as above. The 15, 30, 60 and 120 min annealed WCuBP electrodes demonstrated the OER current density of 252.1, 300, 206.9 and 161.6 at 350 mV fixed overpotential in 1 M KOH.

S-1.7. Faradaic efficiency (FE) of WCuBP

Faradaic efficiency is used to determine the efficiency of electrons transferred to the electrode surface during an electrochemical reaction [13]. It is the ratio of the experimentally generated H_2/O_2 to the theoretically calculated H_2/O_2. FE can be determined using the equation below:

$$Faradaic\ efficiecy = \frac{experimental\ mol\ of\ O_2\ and\ H_2\ gas}{theoretical\ mol\ of\ O_2\ and\ H_2\ gas} \times 100$$

The theoretical value of O_2 or H_2 can be calculated by Faraday's law:

$$n = \frac{I \times t}{z \times F}$$

where n is the number of mol, I is the current in ampere, t is the time in seconds and z is the transfer of electrons (for H_2, z = 2 and for O_2, z = 4). The F is the Faraday constant (96,485 C mol^{-1}). The theoretical values of O_2 and H_2 were calculated at a current of 170 mA for 60 min.

The theoretical value of O_2: n = 1.585 mmol.

The theoretical value of H_2: n = 3.171 mmol.

The generated gas was collected by the water-gas displacement method as shown in Fig. S23. The quantity of O_2 or H_2 was calculated by the following equation:

$$PV = nRT$$

where V is the volume of collected gas, T is the temperature in kelvin, R is the ideal gas constant (0.0821 atm/mol K) and P is the atmospheric pressure (~1 atm).

The number of O_2 in water-gas displacement:

$$(1\ atm)\ (0.03699\ L) = n\left(0.0821\frac{atm}{mol\ K}\right)(298K)$$

$$n = \text{ 1.512 mmol}$$

The number of H_2 in water-gas displacement:

$$(1\ atm)\ (0.0745\ L) = n\left(0.0821\frac{atm}{mol\ K}\right)(298K)$$

$$n = \text{ 3.04 mmol}$$

The faradaic efficiencies of H_2 and O_2 were 96.0% and 95.74%, respectively as shown in Fig. 4(a).

S-1.8. WCuBP electrode: OER oxidation peak

The OER oxidation peak of the optimal WCuBP electrode was analyzed using cyclic voltammetry (CV) within the OER potential range, as shown in Figure S21. In the measured CV, an oxidation peak appeared at 1.44 V while a reduction peak was observed at 1.35 V during the reverse scan. The oxidation and reduction peaks can be attributed to W and Cu. Tungsten (W) has several oxidation states from W^0 to W^{+6} [14]. At the same time, Cu also exhibits highly oxidizing species with oxidation states from Cu^0 to Cu^{III} [15]. The CV process involves 3 different reaction regions. In the first region, hydroxyl groups (OH^-_{ads}) are generated and adsorbed at the initial lower potential, facilitating the activation of active sites for further reactions. In the second region, the transition metals W and Cu in the electrode undergo redox reactions, leading to changes in their oxidation states [16,17]. This oxidation of transition metals in the electrode results in the formation of an oxidation peak [18]. In the third reaction region, desorption of OOH* occurs, leading to oxygen evolution [19]. After the initial oxidation of water molecules and electron transfer at the electrode surface, the reaction intermediates may undergo multiple complex redox reactions, forming various species [19,20]. The interaction of two adsorbed oxygen species on the electrode surface, followed by proton and electron addition, can result in the formation of OOH*. The intermediate OOH* eventually desorbs, resulting in oxygen evolution [21]. The formation of oxide layers can help protect active species by acting as a barrier, which can improve corrosion resistance and increase the durability of the material [22].

S-1.9. After stability characterization

Figure S28 shows the morphological, optical and structural characterization of the post-stability WCuBP electrode, including SEM, XRD, XPS and Raman analysis. The SEM images of WCuBP MLC before and after stability are shown in Figures S28(a) – S28(a-1). The morphological structure

showed no significant degradation but the leaf edges appeared slightly rougher. The XRD pattern comparison of WCuBP before and after the stability is shown in Figure S28(b). After the stability test, a noticeable decrease in peak intensity was observed and most secondary peaks disappeared due to the formation of oxidation states, which can affect the local crystal structure and lead to surface reconstruction. The XPS analysis of the WCuBP electrode before the stability test is shown in Figures 2(c) – 2(c-4). XPS analysis was performed on the WCuBP electrode after the stability test to investigate changes in chemical composition and surface chemistry. The full scan spectrum after the stability test is shown in Figure S28(c), which confirms the existence of W 4f, Cu 2P, B 1s and P 2p phase peaks. In the W 4f spectrum, the increased intensity of the W $4f_{5/2}$ peak indicated a change in the chemical state of tungsten, which can be associated with the formation of W^{6+} oxidation states [23]. The Cu 2p spectrum indicated an increase in the CuO peaks. B 1s and P 2p also exhibited a higher portion of oxidation species after the stability test, as shown in Figures S28(c-3) – S28(c-4). Overall, the high-resolution post-stability XPS spectra showed decreased elemental peaks and increased oxide/hydroxide species, indicating surface transformation due to oxidation and the adsorption of O-containing intermediates. The Raman spectra comparison of WCuBP is shown in Figure S28(d). Reduced peak intensity observed for all the Raman characteristic peaks can be attributed to the local phase transformation, which can affect the intensity of the defined vibrational modes. Overall, post-stability physical characterizations showed surface oxidation, commonly observed in prolonged redox processes. This surface oxidation can facilitate the introduction of active sites and ensure stability [24].

S-2. WCuBP micro-leaf cluster (MLC) electrocatalysts

S-2.1. Substrate and other necessary characterizations

S-2.1.1. Bare nickel foam characterization

S-2.1.2. Synthesis of WCuBP electrode

S-2.1.5. Benchmark electrode: Pt/C

S-2.1.6. Benchmark electrode: RuO_2

S-2.2. Optimization of WCuBP electrode

S-2.2.1. Reaction time variation

S-2.2.2. W concentration variation

S-2.2.3. Reaction temperature variation

S-2.2.4. Post-annealing temperature variation

S-2.2.5. Post-annealing duration variation

S-2.3 Before and after post-annealing analysis: LSV

S-2.4 WCuBP and CuBP LSV comparision

S-2.1.1. Bare nickel foam characterization

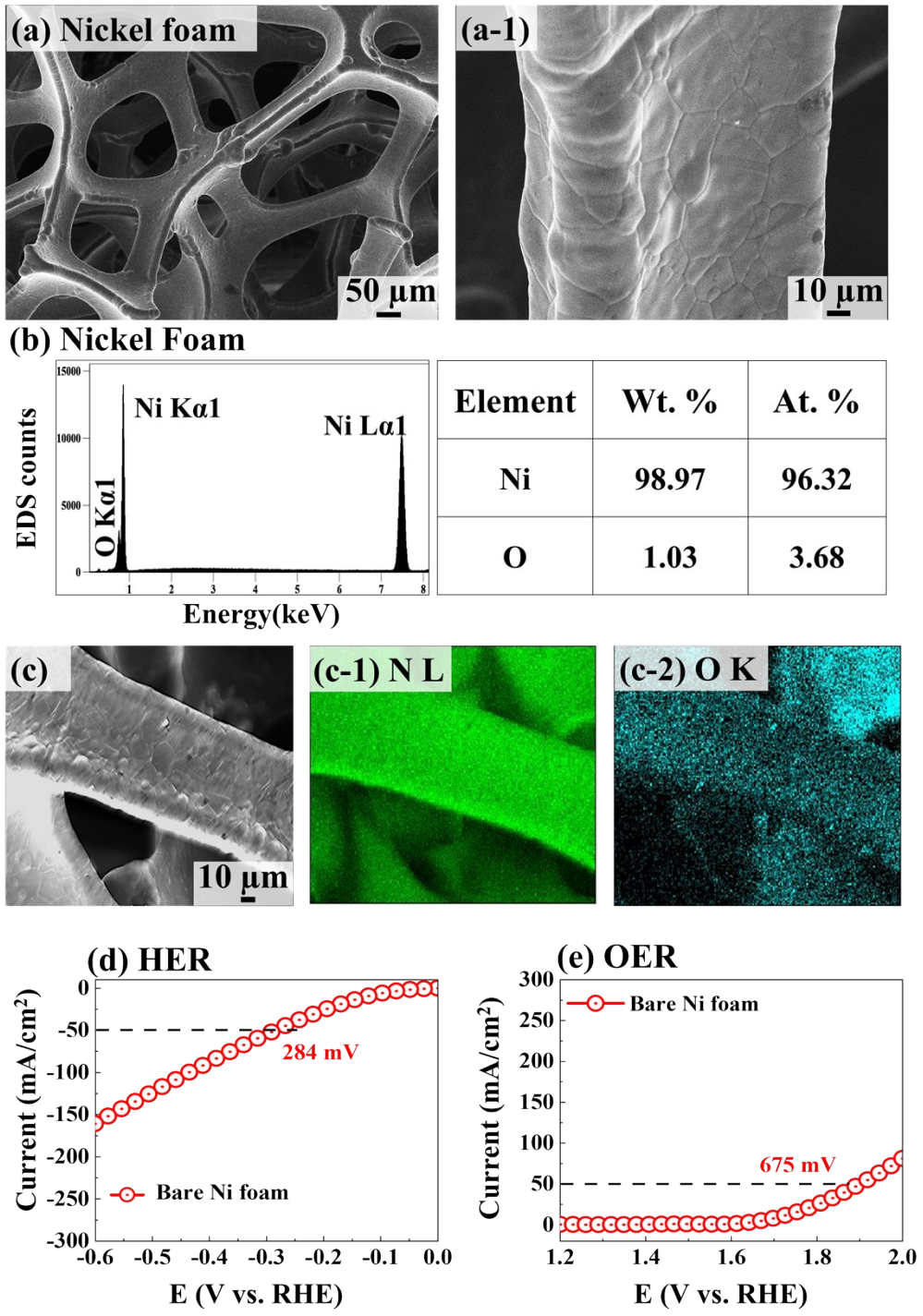

Figure S1. (a) – (a-1) SEM image of bare Ni foam (NF) substrate. (b) EDS spectra with atomic percentage table. (c) – (c-2) EDS maps of bare NF. (d) – (e) HER/OER LSV curves of NF in 1 M KOH.

S-2.1.2. Synthesis of WCuBP electrode

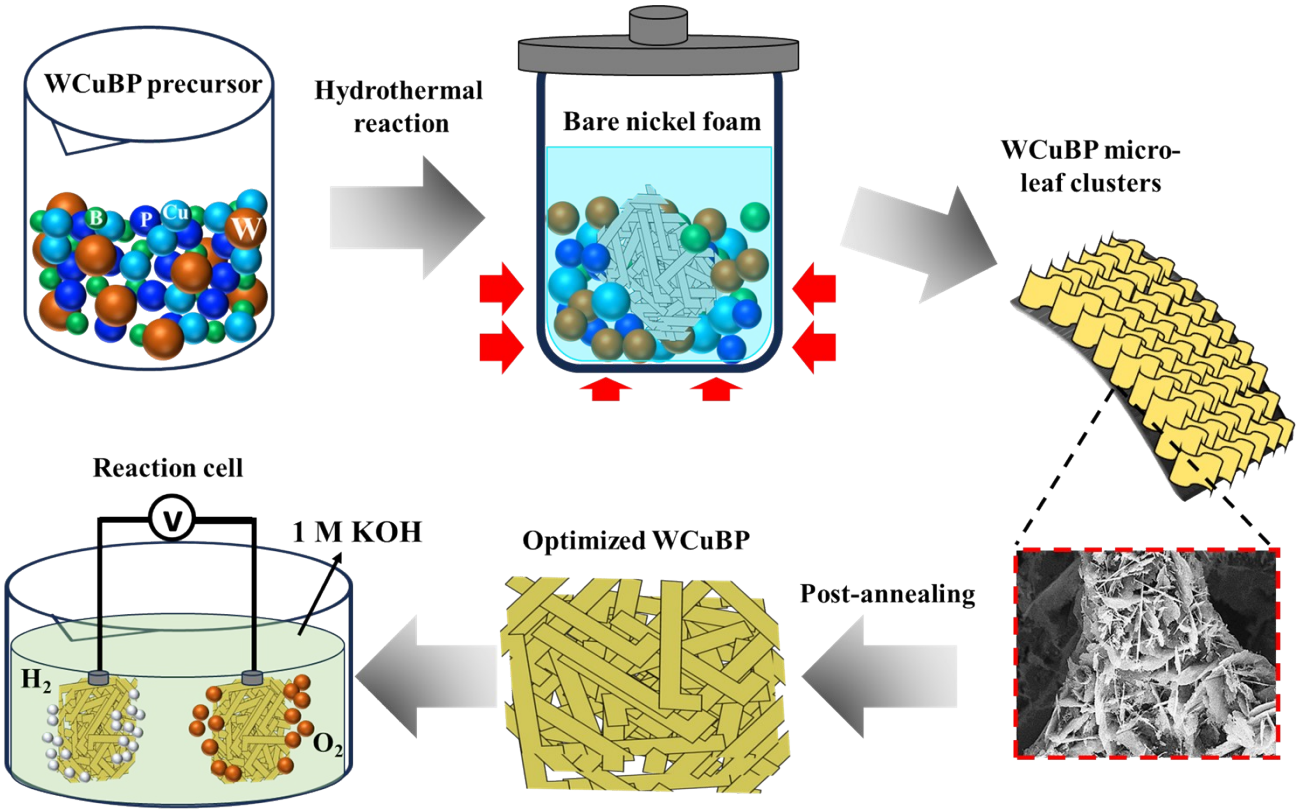

Figure S2. Single-step hydrothermal synthesis process of WCuBP micro-leaf cluster. For WCuBP fabrication, the precursor was deposited onto bare nickel foam through a single-step hydrothermal method. Later, hydrothermally prepared WCuBP was post-annealed to enhance its crystal structure and electrocatalytic performance. Detailed discussion about WCuBP fabrication can be found in Supplementary S-1.2.

S-2.1.3. Pt/C benchmark analysis

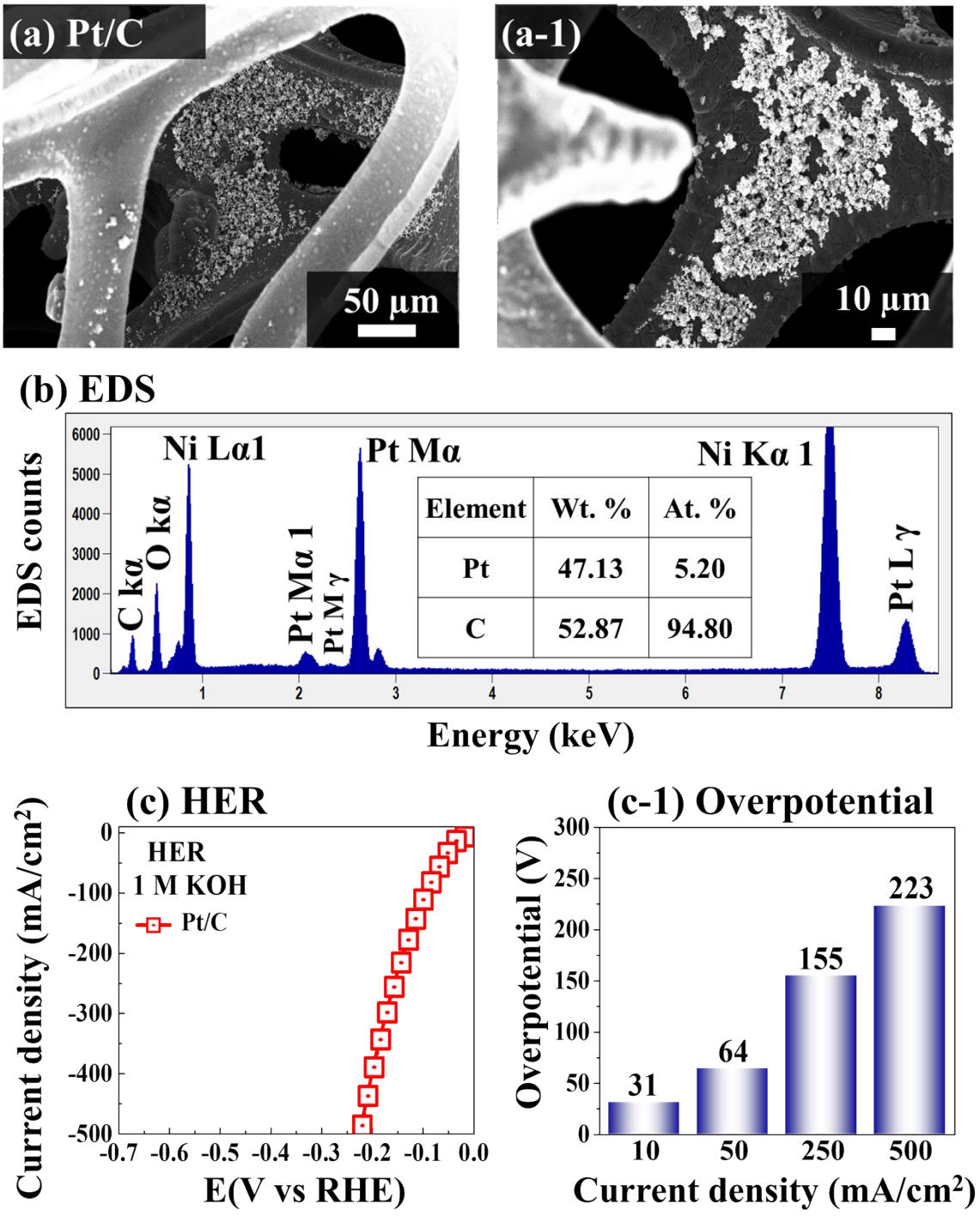

Figure S3. (a) – (a-1) SEM image of HER benchmark (Pt/C). (b) EDS spectra with atomic percentage table. (c) – (c-1) HER LSV curve and overpotential graph of Pt/C at different current densities.

S-2.1.4. RuO_2 benchmark analysis

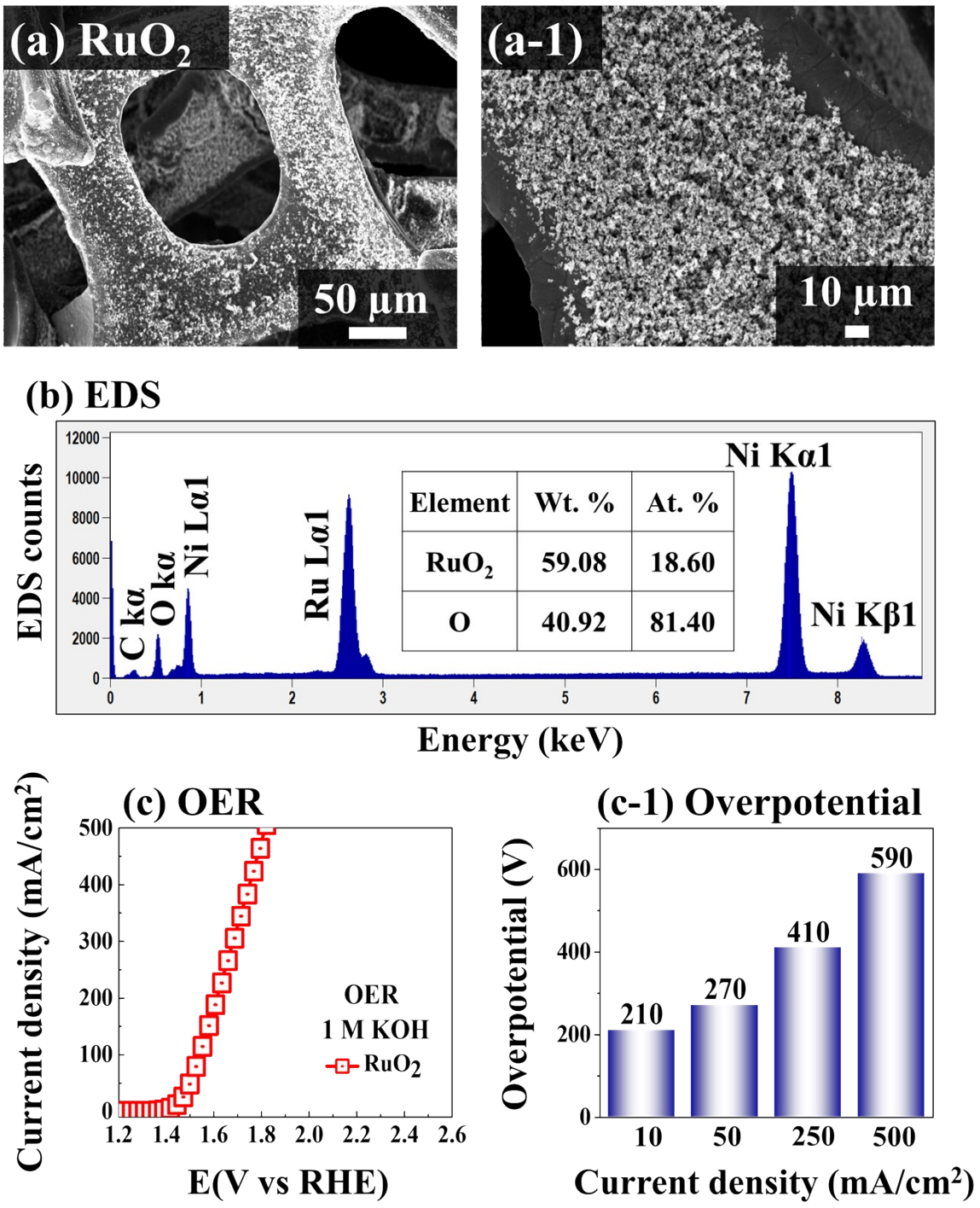

Figure S4. (a) – (a-1) SEM image of RuO_2 electrode (b) EDS spectra with atomic percentage table. (c) – (c-1) OER LSV curve of RuO_2 and overpotential graph at different current densities.

S-2.1.5. Scan rate optimization for WCuBP electrode

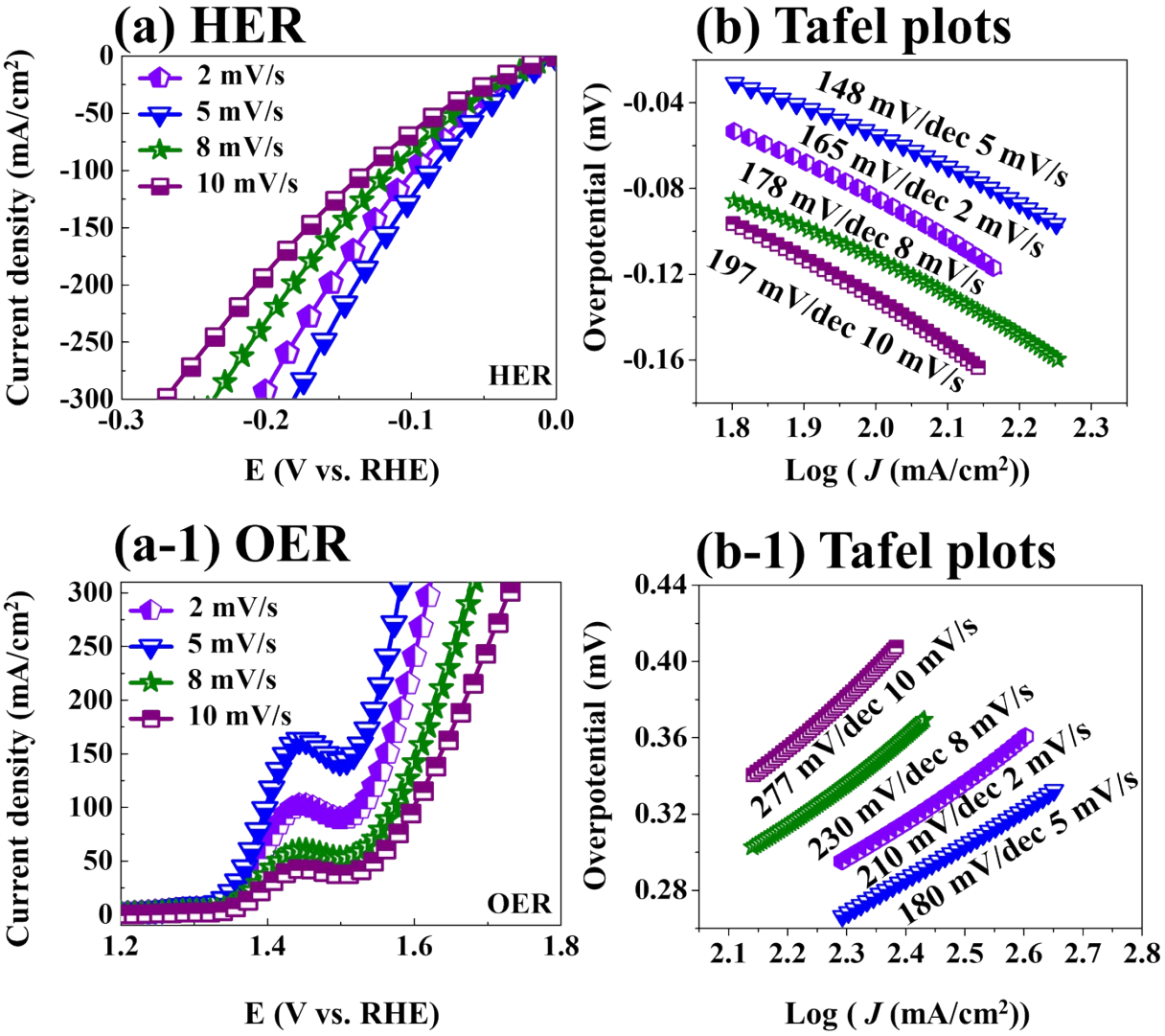

Figure S5. Different scan rate optimization for the WCuBP electrode fabrication. (a) – (a-1) HER and OER performance at different scan rates. (b) – (b-1) Tafel slopes of corresponding HER/OER LSV curves.

S-2.1.6. EIS measurements at different voltage

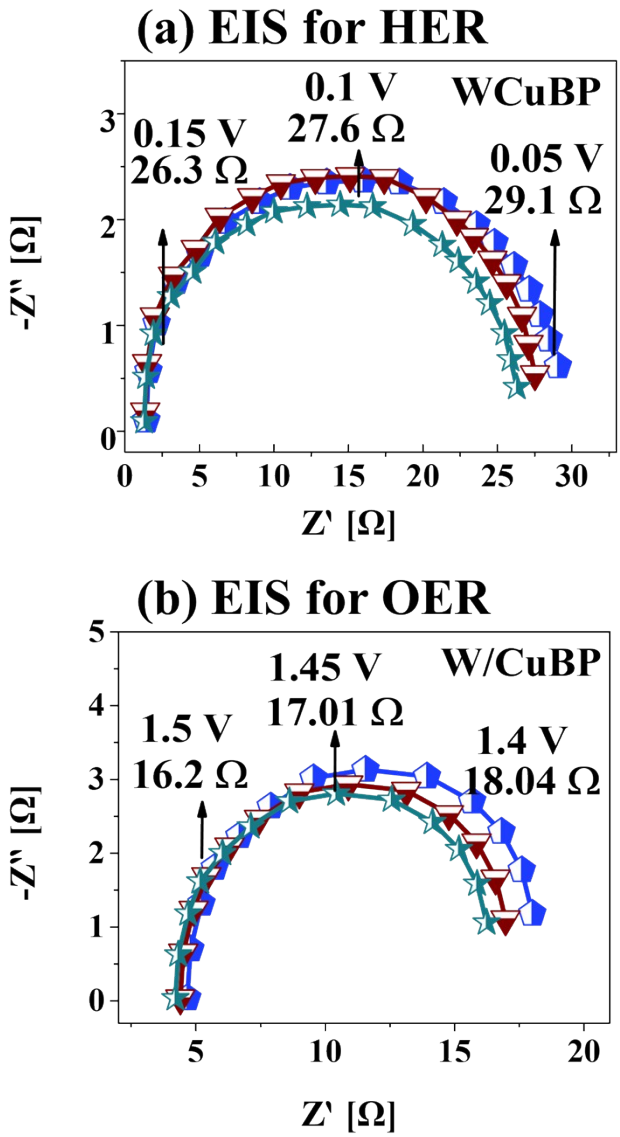

Figure S6. Electrochemical Impedance Spectroscopy (EIS) of the best WCuBP electrode at different applied voltages. (a) HER EIS. (b) OER EIS. The R_{ct} value varies at different voltages around the turnover region [25]. The higher applied voltages result in lower R_{ct} values. For consistency, the EIS current density was fixed at 15 mA/cm^2 around the turnover region for all samples between 100 kHz to 0.1 Hz with an amplitude of 5 mV.

S-2.2.1. Reaction time variation

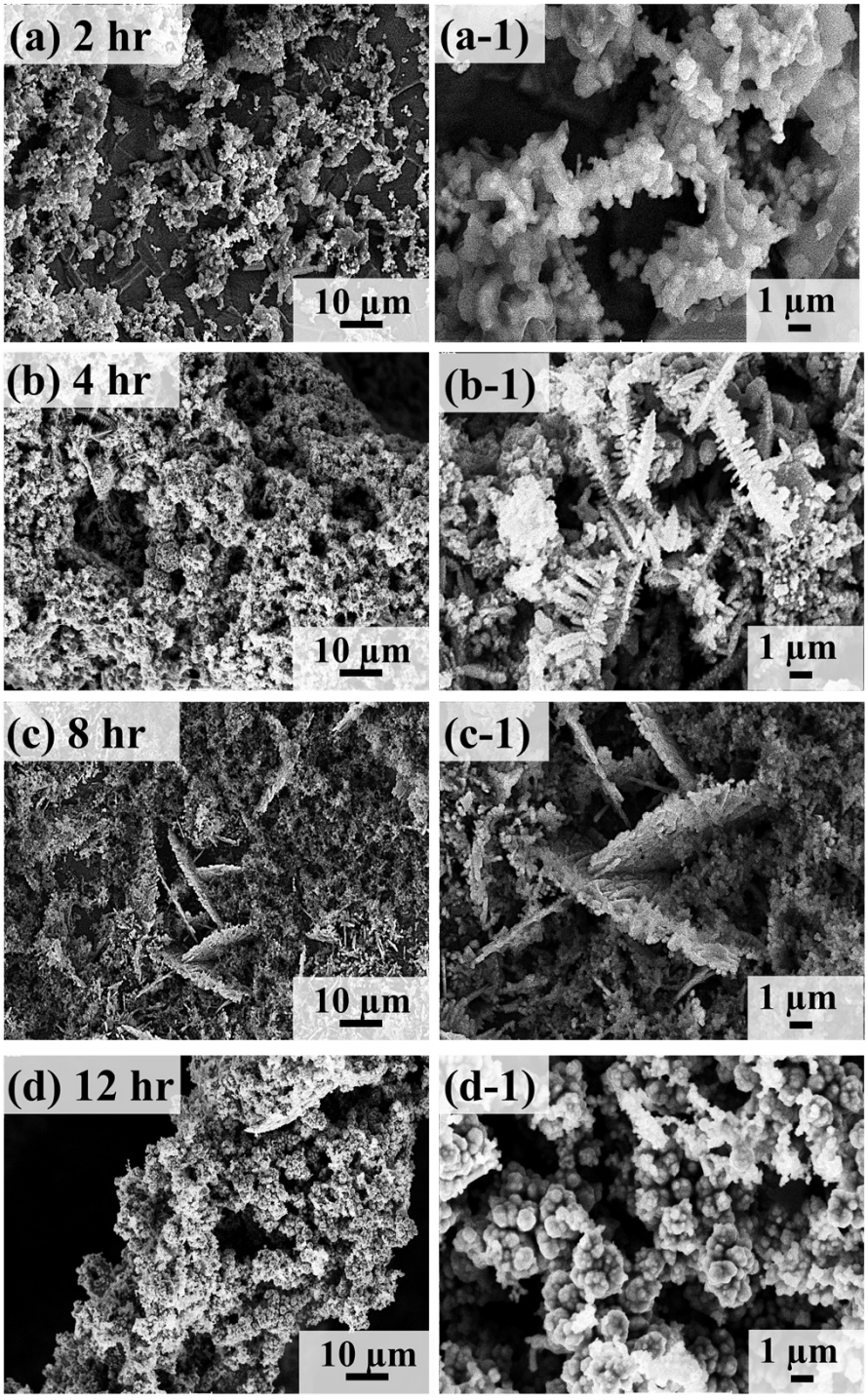

Figure S7. (a) – (d) SEM images of hydrothermal reaction time variation set of WCuBP electrode. The reaction time varied between 2 ~ 12 hours. (a-1) – (d-1) Zoom in images.

S-2.2.1. Reaction time variation

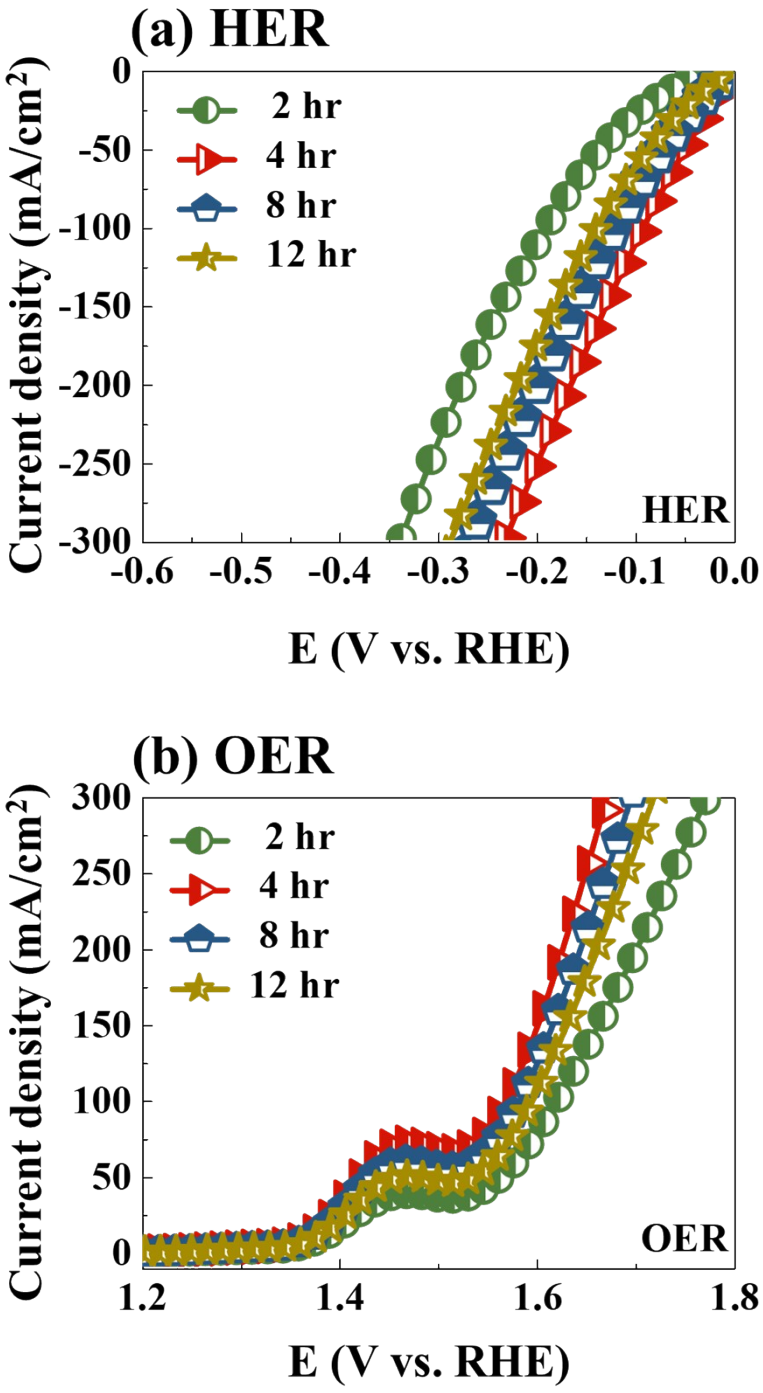

Figure S8. Electrochemical characterization of hydrothermal reaction time variation set of WCuBP electrodes. (a) HER LSV curves. (b) OER LSV curves. The 4 hour reaction demonstrated better HER and OER performance in this set.

S-2.2.2. W concentration variation

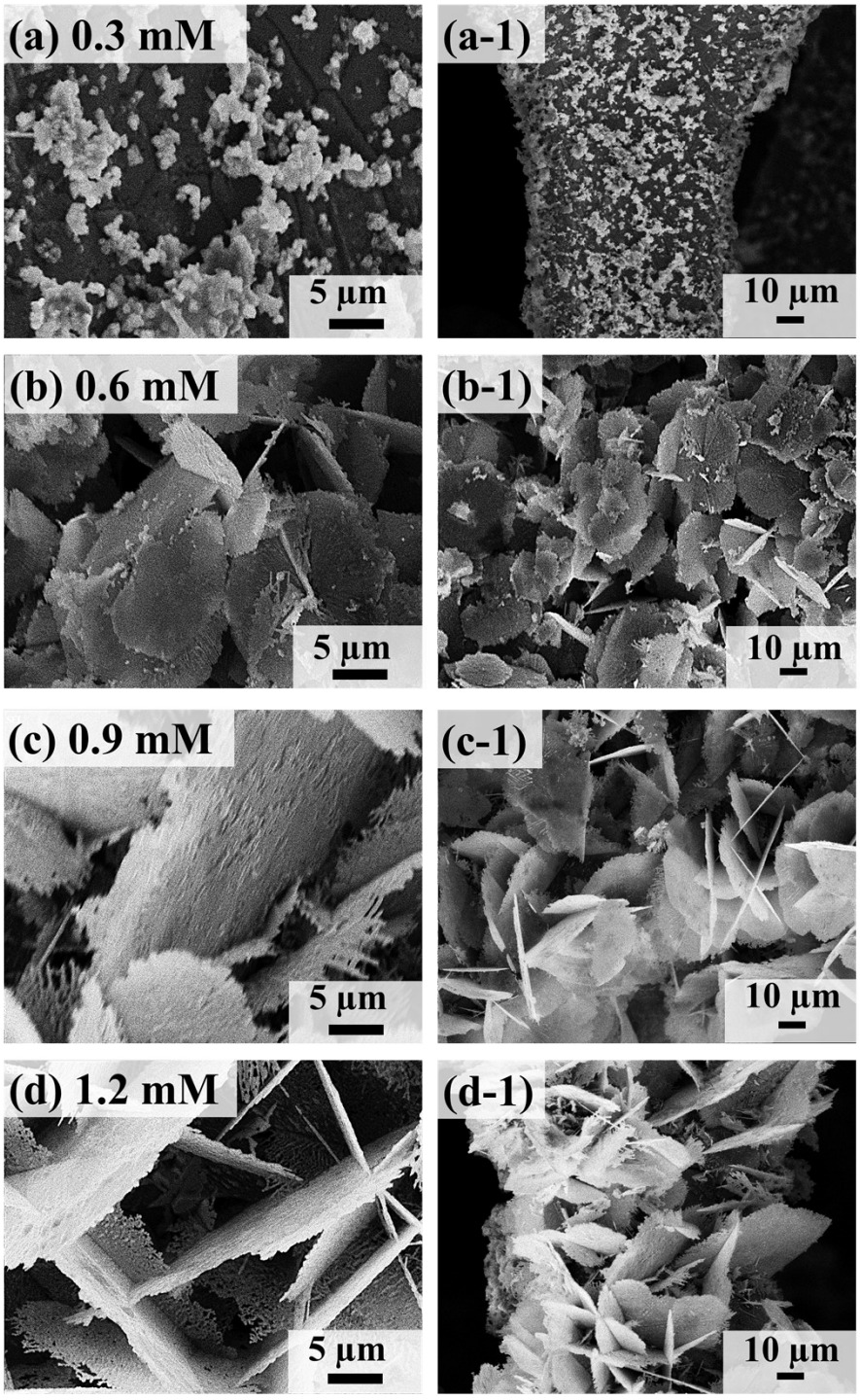

Figure S9. (a) – (d) SEM images of W concentration variation set for the fabrication of WCuBP electrode. The concentration was varied between 0.3 mM to 1.2 mM for 4 hour. (a-1) – (d-1) Zoom in images.

S-2.2.2. W concentration variation

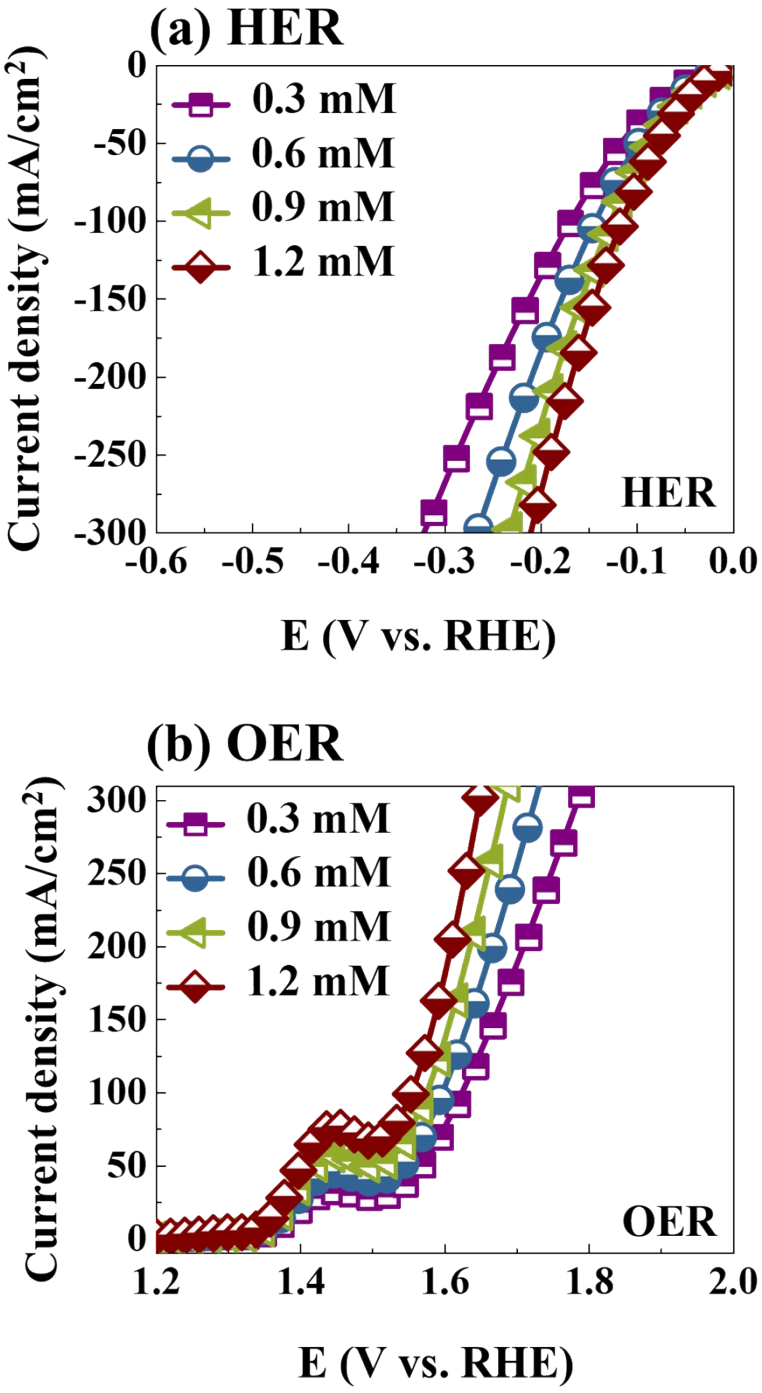

Figure S10. Electrochemical characterization of W concentration variation set. (a) HER polarization curves. (b) OER polarization curves. The 1.2 mM W concentration exhibited the best HER and OER activity in this set.

S-2.2.3. Reaction temperature variation

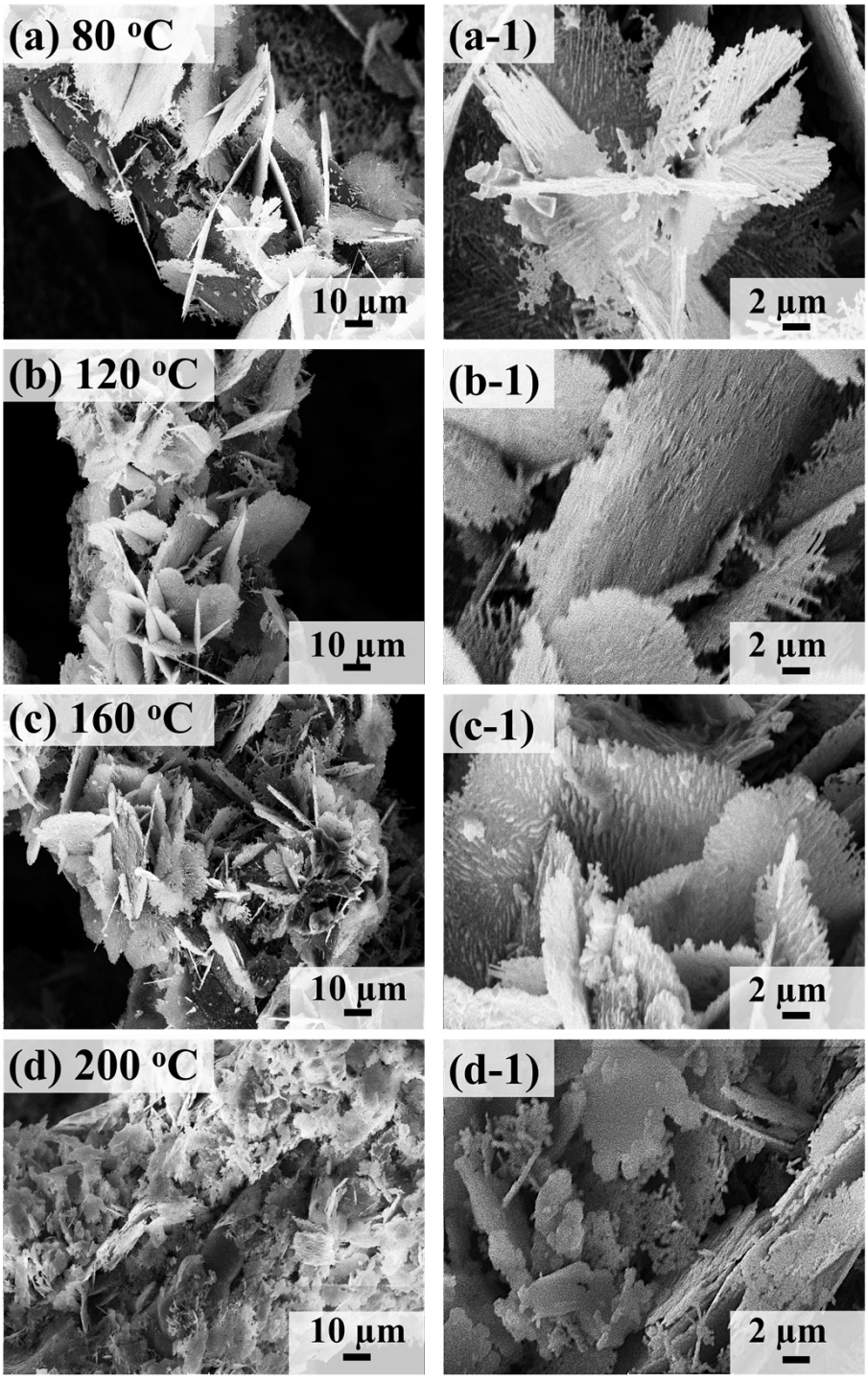

Figure S11. (a) – (d-1) SEM images of hydrothermal reaction temperature variation set for the fabrication of WCuBP electrode. The temperature varied from 80 ~ 200 ℃ for 4 hour with 1.2 mM W concentration. (a-1) – (d-1) Zoom in images.

S-2.2.3. Reaction temperature variation

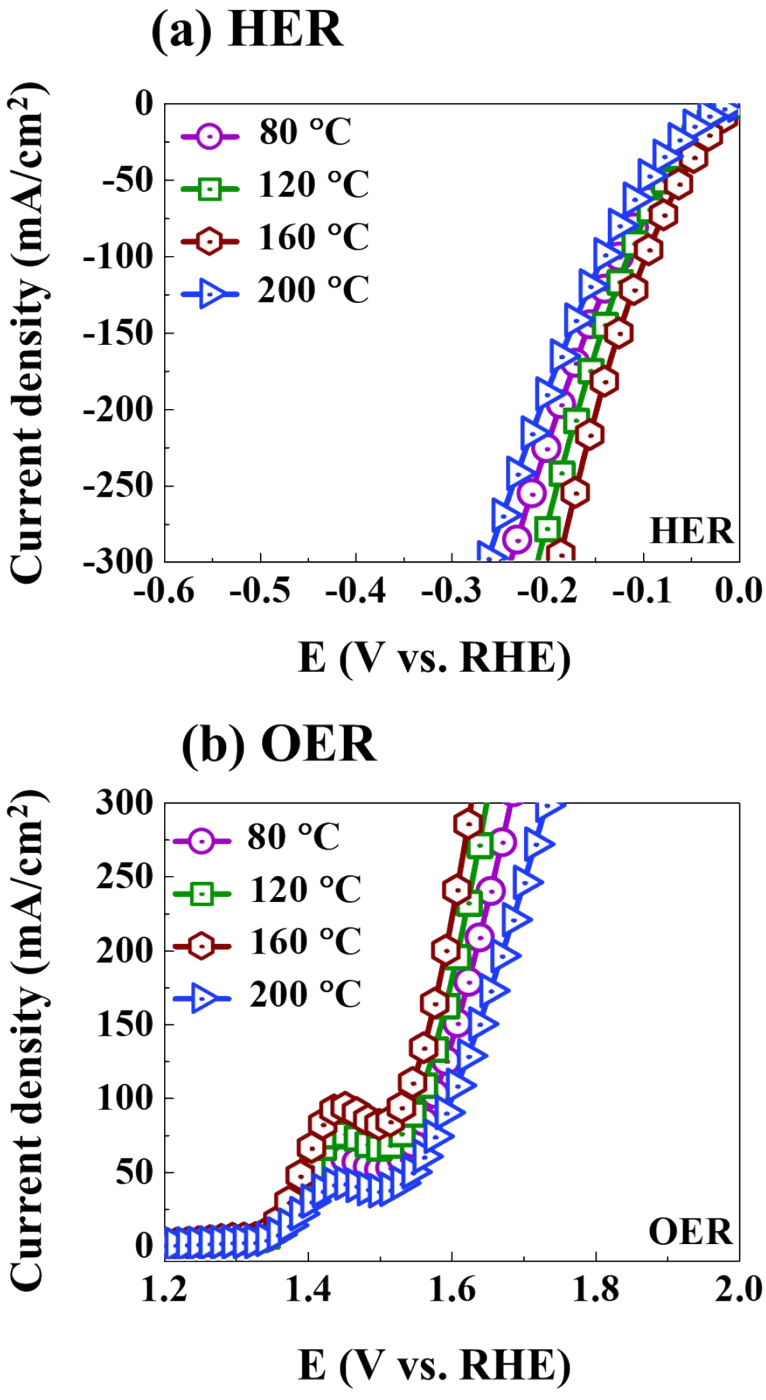

Figure S12. Electrochemical characterization of hydrothermal reaction temperature variation set. (a) HER polarization curves. (b) OER polarization curves. The electrode fabricated at the reaction temperature of 160 ℃ exhibited the best performance for both HER and OER in this set.

S-2.2.4. Post-annealing temperature variation

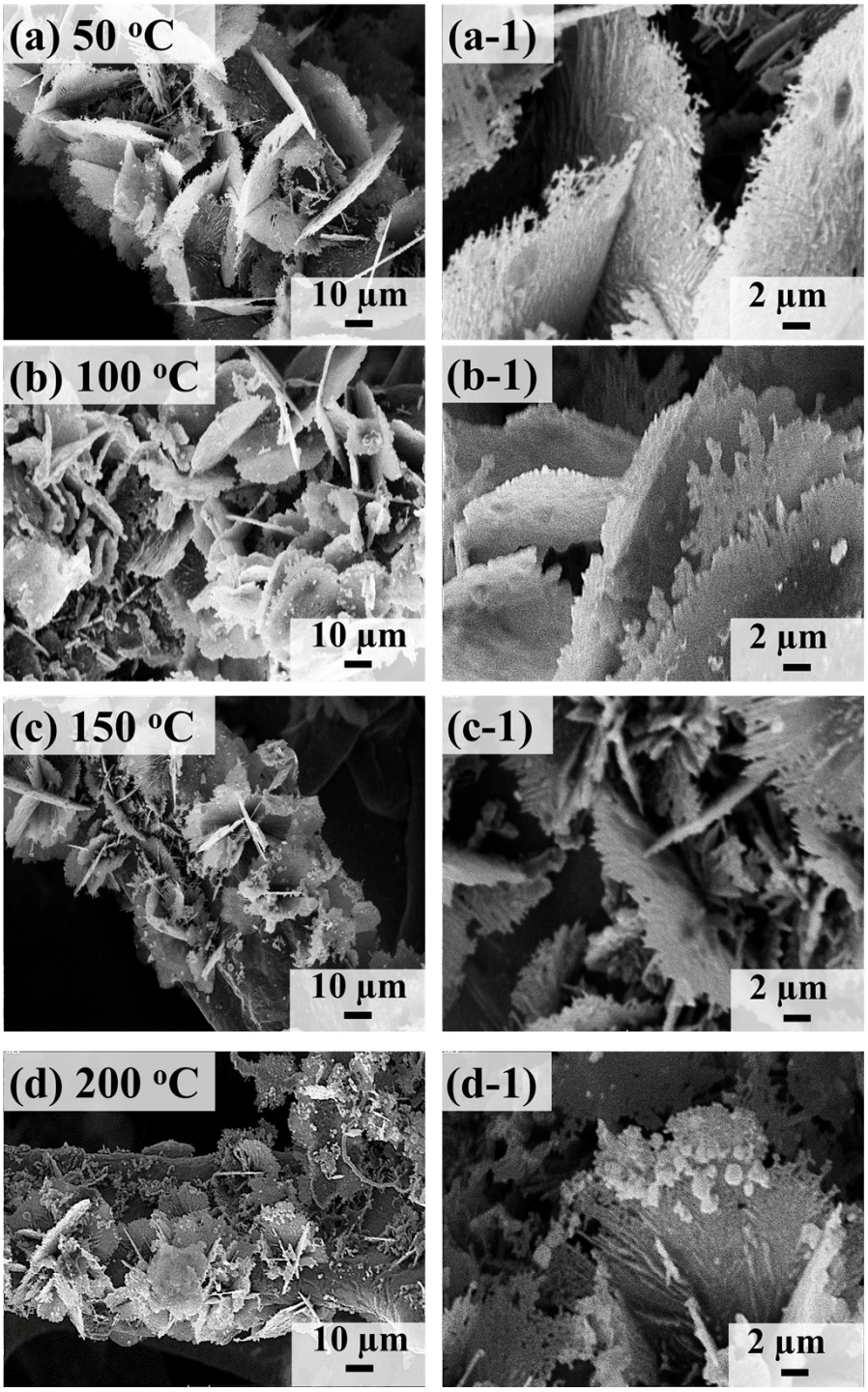

Figure S13. (a) – (d) SEM images of WCuBP post-annealing temperature variation set. Initially, the optimal WCuBP electrode with 1.2 mM W concentration was hydrothermally prepared for 4 hours at 160 ℃. Later post annealed temperature was varied between 50 ~ 200 ℃. (a-1) – (d-1) Zoom-in images of corresponding samples.

S-2.2.4. Post-annealing temperature variation

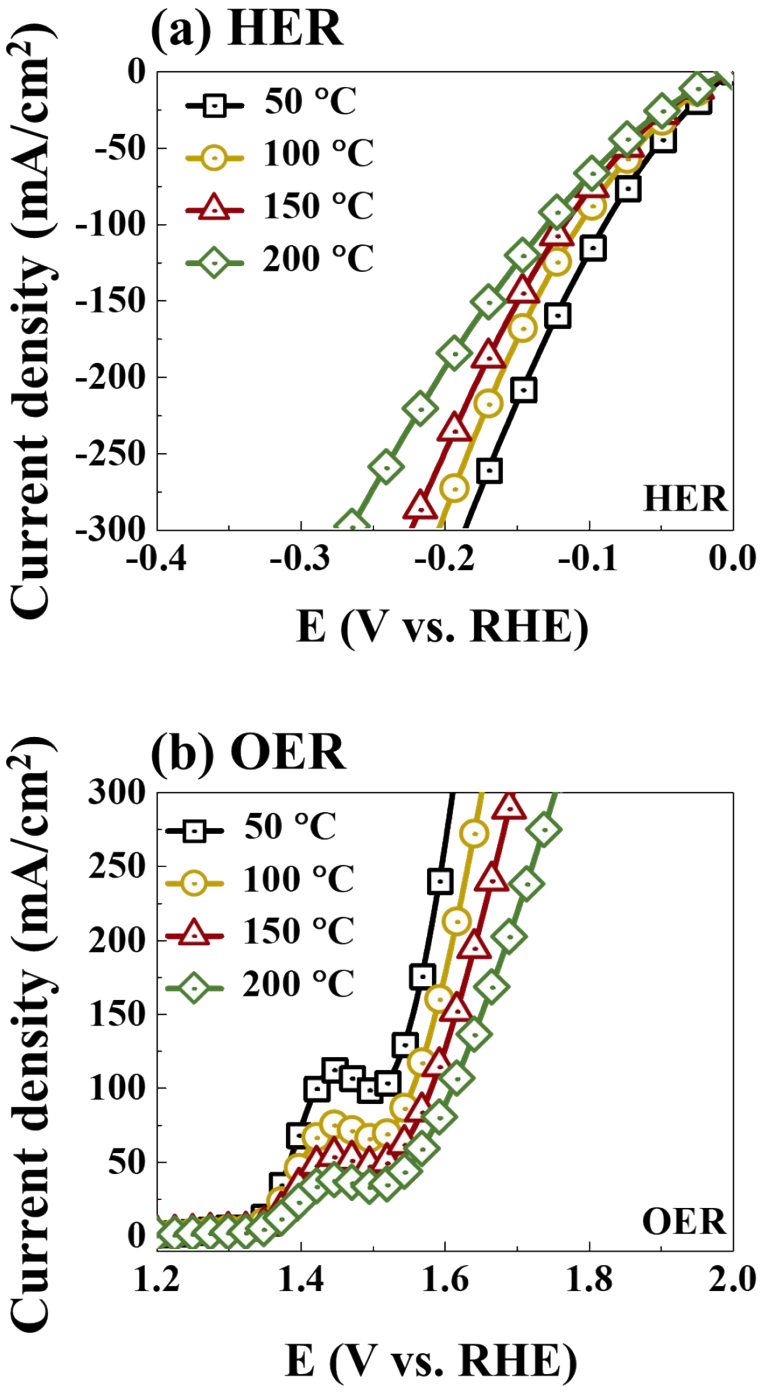

Figure S14. Electrochemical characterization of WCuBP post-annealing temperature variation set. (a) HER polarization curves. (b) OER polarization curves. The electrode post-annealed at 50 ℃ shows the best electrochemical performance in terms of HER and OER in this set.

S-2.2.5. Post-annealing duration variation

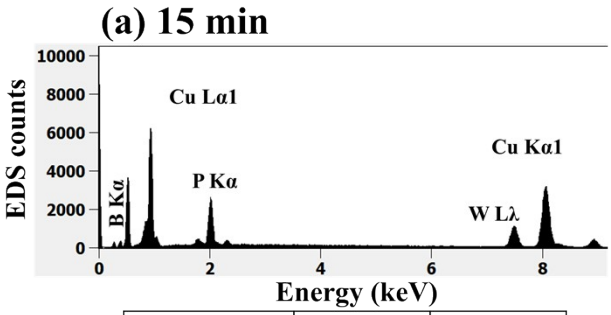

Element	Wt. %	At. %
W	31.48	11.52
Cu	63.91	67.65
B	2.67	16.61
P	1.94	4.21

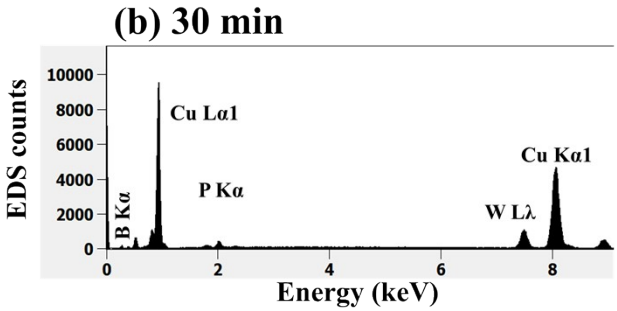

Element	Wt. %	At. %
W	30.71	11.31
Cu	64.06	68.24
B	2.37	14.84
P	2.57	5.62

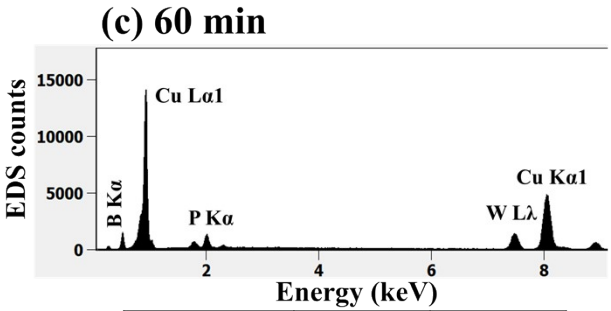

Element	Wt. %	At. %
W	31.37	11.54
Cu	63.95	68.09
B	2.49	15.58
P	2.19	4.78

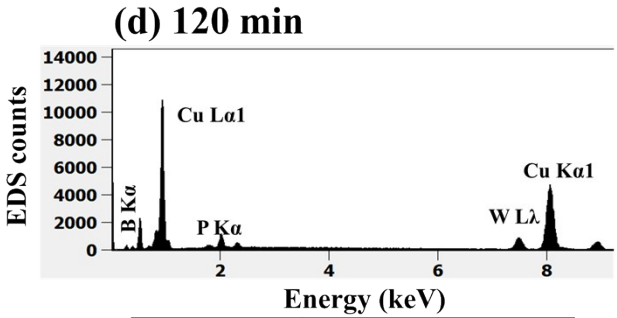

Element	Wt. %	At. %
W	31.84	11.68
Cu	63.72	67.64
B	2.71	16.91
P	1.73	3.77

Figure S15. (a) – (d) EDS spectra of WCuBP for post-annealing duration variation set with atomic and weight percentage tables of each element.

S-2.2.5. Post-annealing duration variation

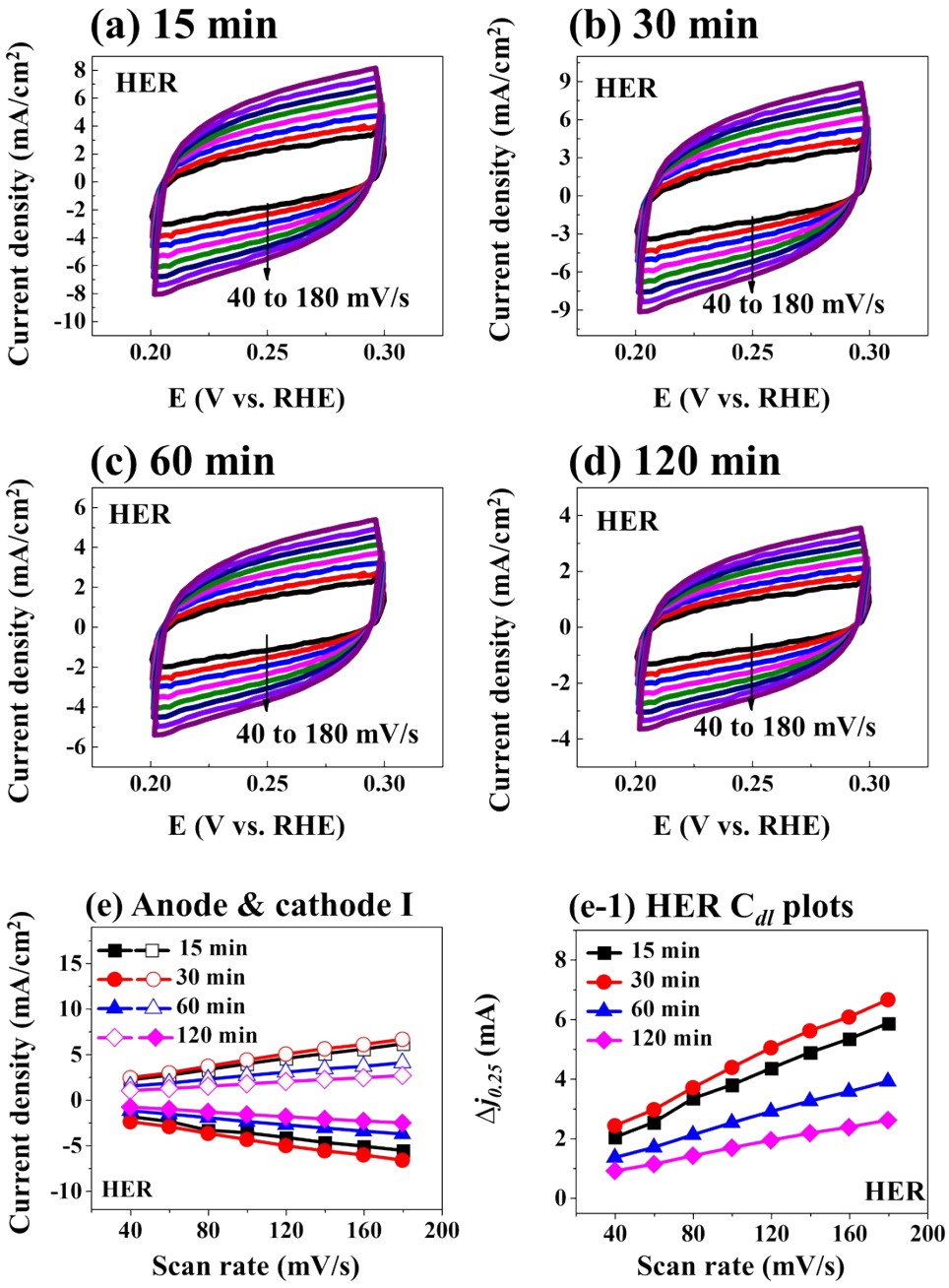

Figure S16. (a) – (d) HER CV curves of post-annealing duration variation set. The CV curves were measured in non-faradic regions where no charge transfer reactions take place, between 0.2 to 0.3 and below 1.023 V based on the equation $E_{RHE} = E + 0.059 * pH + 0.197$ (Ag/AgCl) [26]. The Actual value of reverse swing voltage (E) was – 0.723 and -0.823 V. The scan rate varied from 40 to 180 mV/s. (e) HER anodic and cathodic current density plots as a function of scan rate. (e-1) HER double-layer capacitance (C_{dl}) plots.

S-2.2.5. Post-annealing duration variation

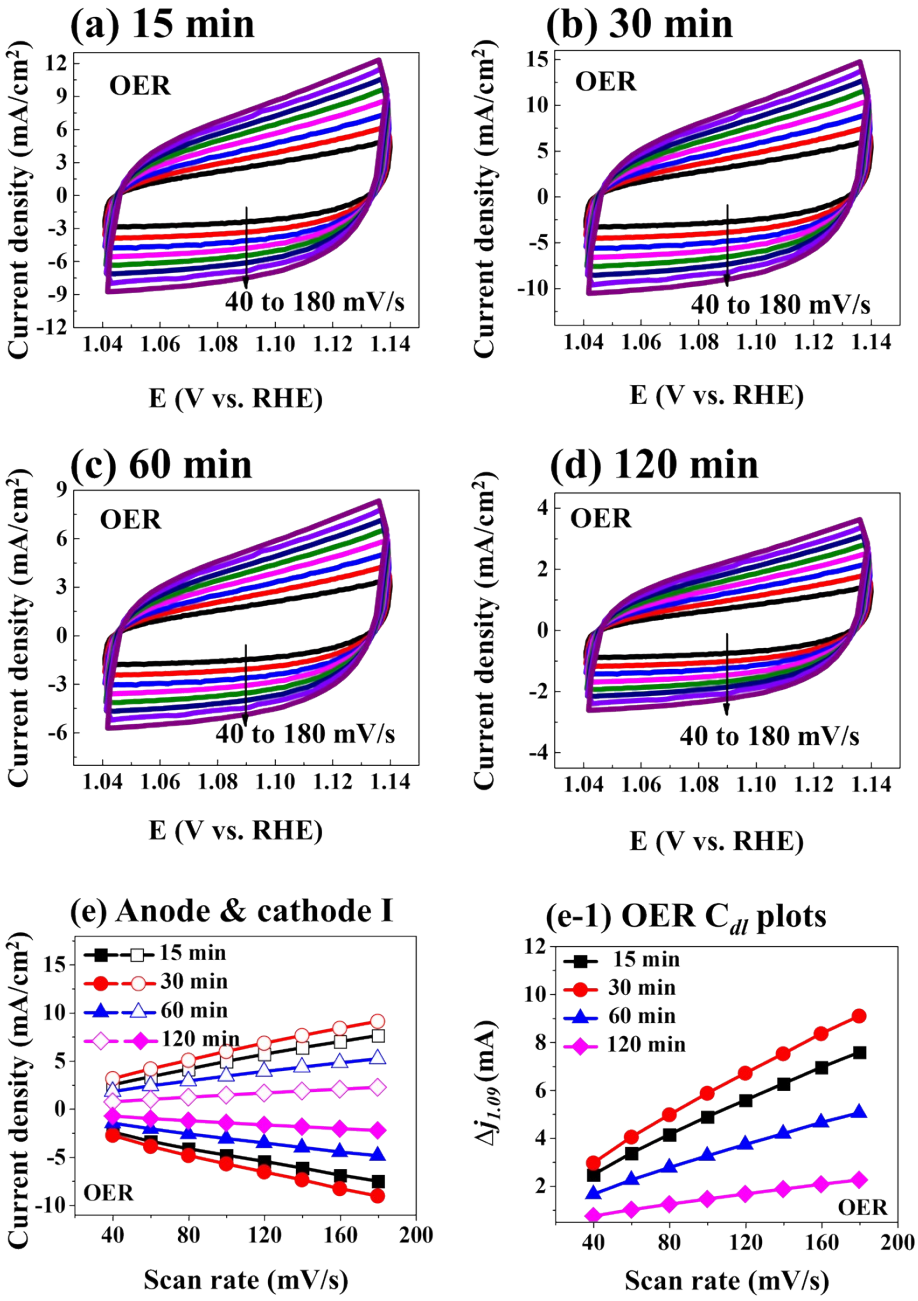

Figure S17. (a) – (d) OER CV curves of post-annealing duration variation set. The CV curves were measured in non-faradic regions where no charge transfer reaction occurs between 1.04 to 1.14 and below 1. 23 V based on the equation $E_{RHE} = E + 0.059 * pH + 0.197$ (Ag/AgCl) [27]. The Actual value of sweeping voltage (E) was 0.017 and 0.117 V. The scan rate varied from 40 to 180 mV/s. (e) OER anodic and cathodic current density plots as a function of scan rate. (e-1) OER double-layer capacitance (C_{dl}) plots.

S-2.2.5. Post-annealing duration variation: ECSA

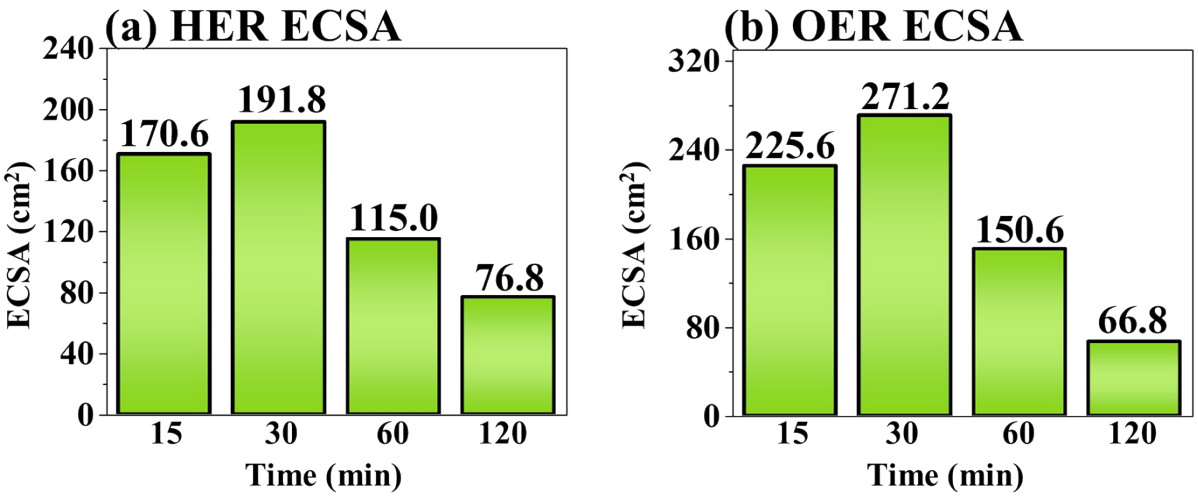

Figure S18. (a) – (b) HER and OER ECSA values of WCuBP.

S-2.3 Before and after post-annealing analysis: LSV

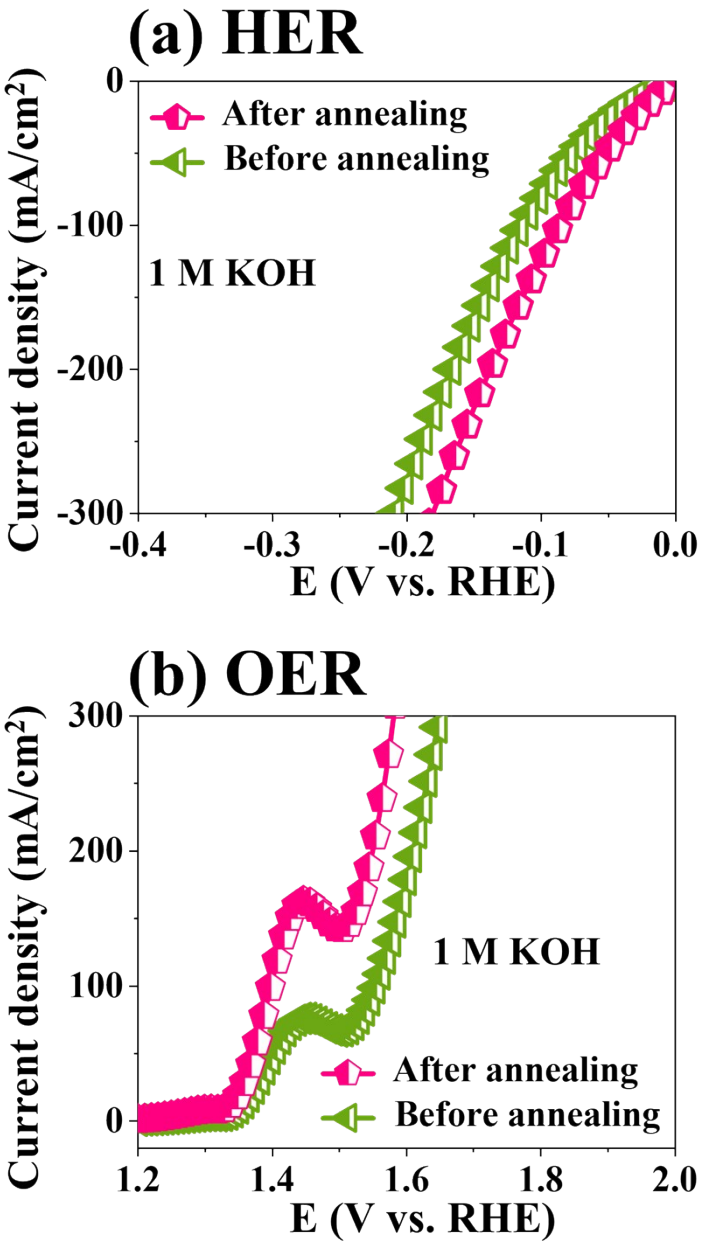

Figure S19. (a) – (b) Before and after post-annealing LSV comparison of WCuBP.

S-2.4 WCuBP and CuBP LSV comparison

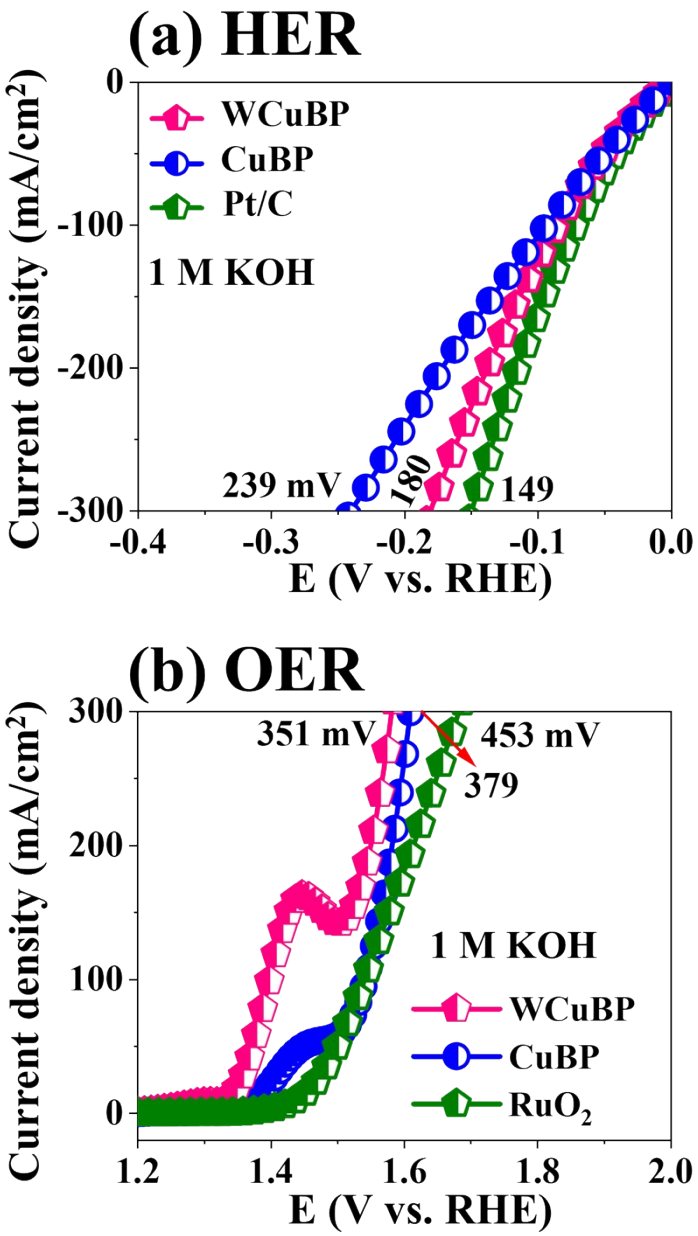

Figure S20. (a) – (b) HER and OER activity of WCuBP, CuBP and benchmark electrodes (Pt/C and RuO_2).

S-3. Analysis of the best WCuBP electrode

S-3.1. Full scan of CV measurement

S-3.2. HER/OER repeatability test

S-3.3. HER steady-state measurements

S-3.4. OER steady-state measurements

S-3.5. Water-gas displacement setup

S-3.6. HER/OER activity of WCuBP and bare NF

S-3.7. 2-E natural water performance

S-3.1. CV measurement in OER region

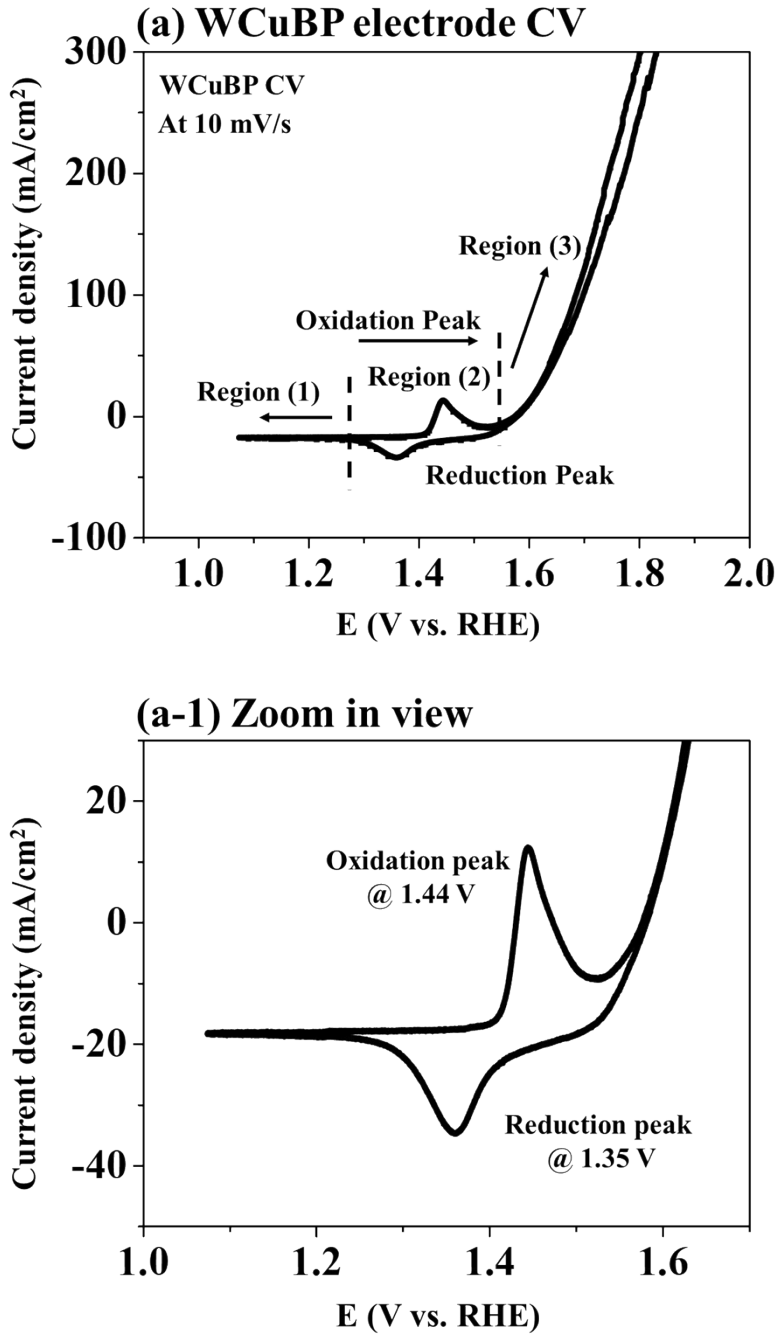

Figure S21. (a) OER CV curves of the WCuBP electrode at scan rate 10 mV/s in the same OER range. It demonstrated the presence of an oxidation peak at 1.44 V below the turnover region and a reduction peak at 1.35 V. (a-1) Zoom in view. Detailed discussion related to the OER oxidation peak can be found in S-1.8 (WCuBP electrode: OER oxidation peak).

S-3.2. HER/OER repeatability test

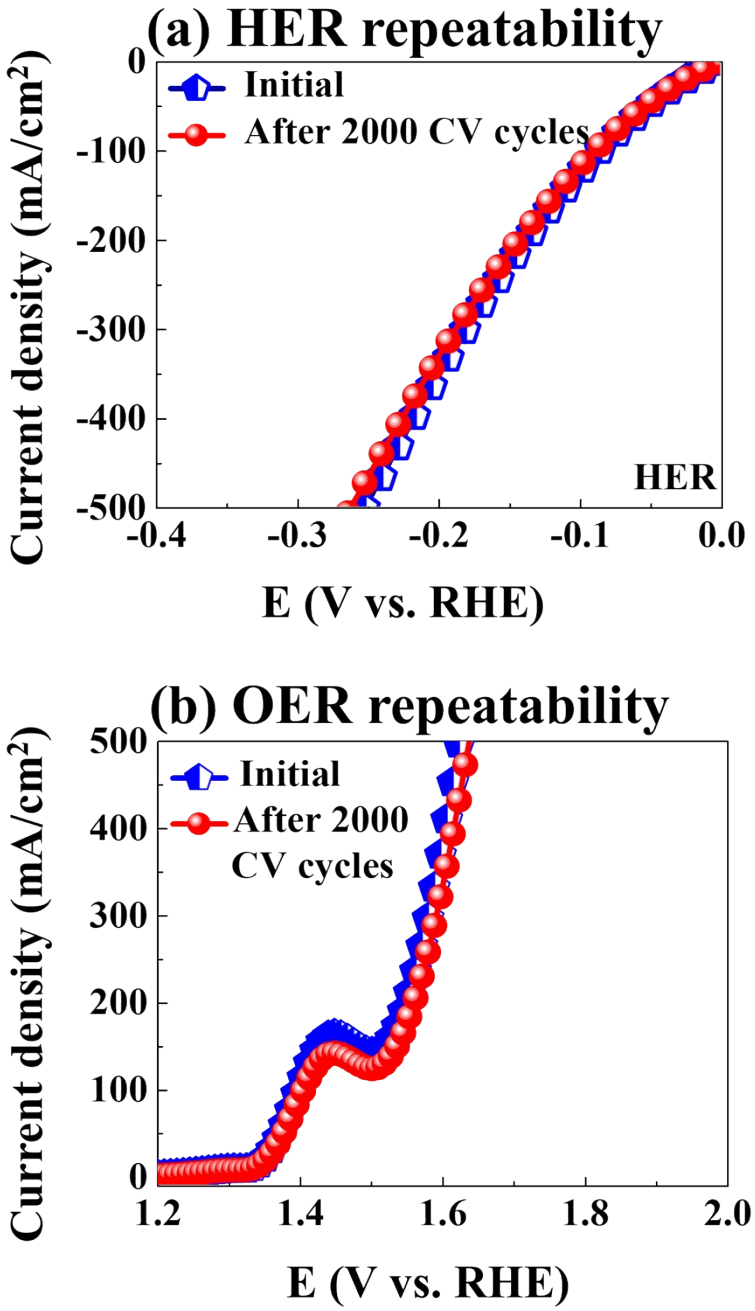

Figure S22. 3-E repeatability test in 1 M KOH for 20 hours after 2000 CV cycles. (a) HER repeatability test. (b) OER repeatability test.

S-3.3. HER steady state measurements

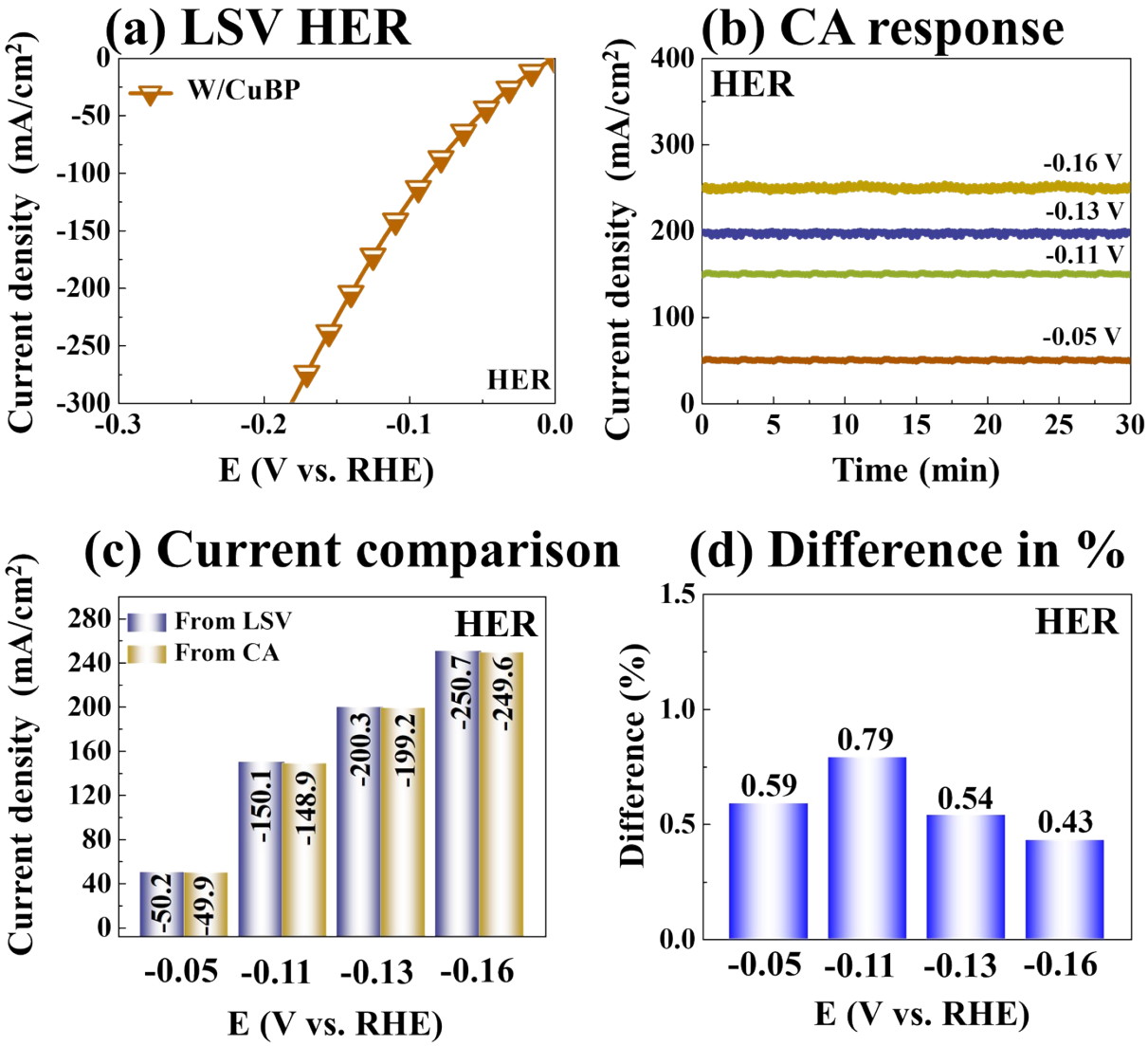

Figure S23. HER 3-electrode steady-state measurements of WCuBP electrode in 1 M KOH. (a) HER LSV. (b) HER CA response at – 0.05 V, - 0.11, - 0.13 and - 0.16 V. (c) Comparison of LSV and CA current. (d) The current difference between the LSV curve and CA response in percentage.

S-3.4. OER steady-state measurements

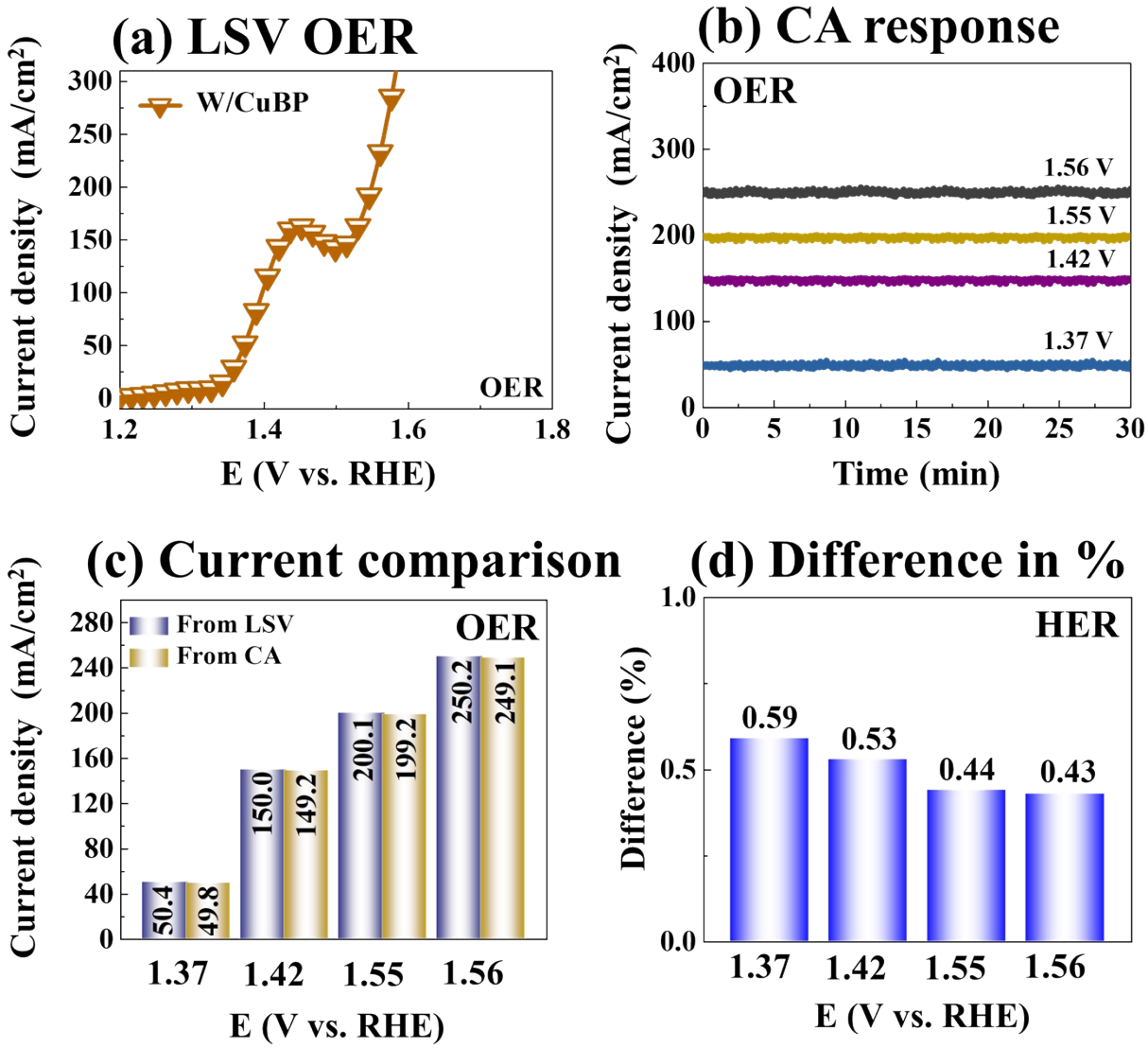

Figure S24. OER 3-electrode steady-state measurements in 1 M KOH of WCuBP electrode. (a) OER LSV. (b) OER CA response at 1.37, 1.42, 1.55 and 1.56 V. (c) Comparison of LSV and CA current. (d) The current difference between the LSV curve and CA performance in percentages.

S-3.5. Water-gas displacement setup

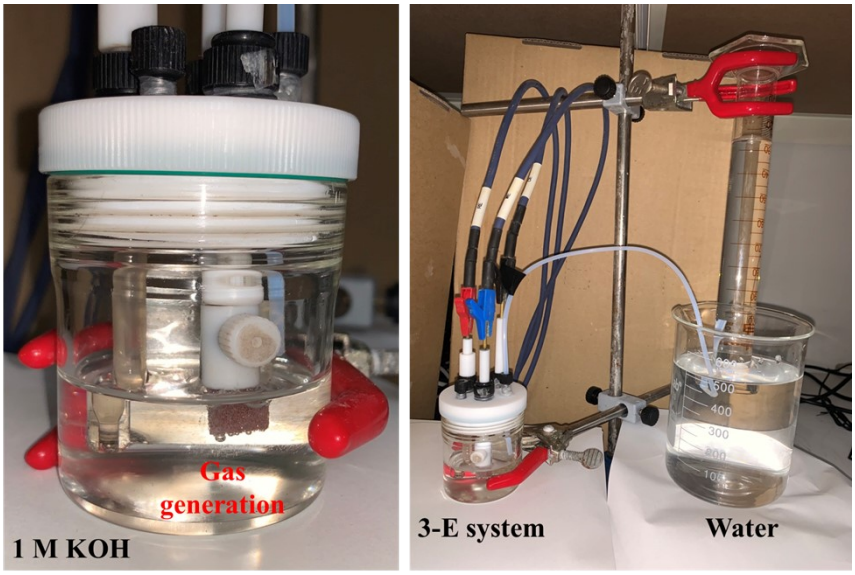

Figure S25. Faradaic efficiency measurement of WCuBP MLC. Water-gas displacement setup in 1 M KOH.

S-3.6. HER/OER activity of WCuBP and bare NF

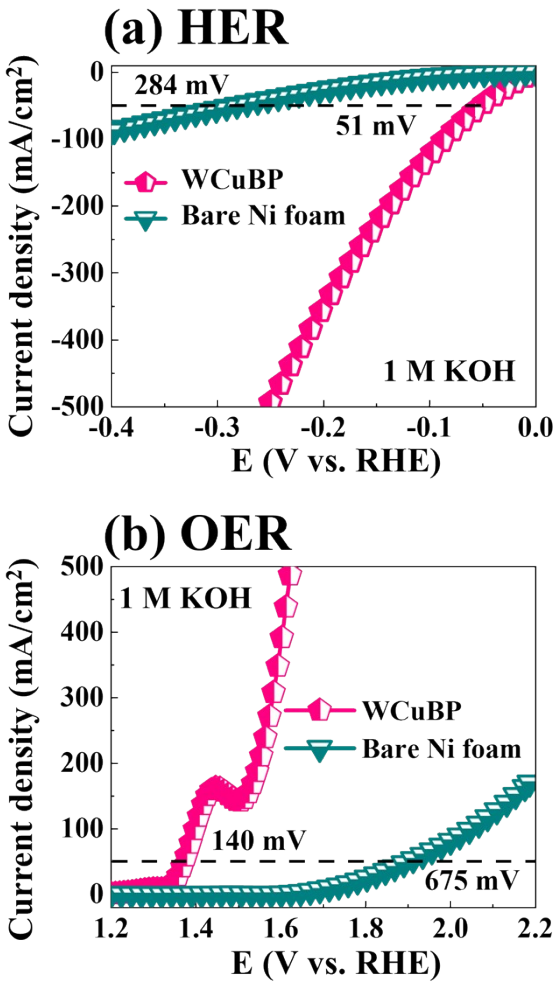

Figure S26. (a) – (b) HER/OER activity comparison of bare NF and WCuBP in 1 M KOH.

S-3.7. 2-E natural water performance

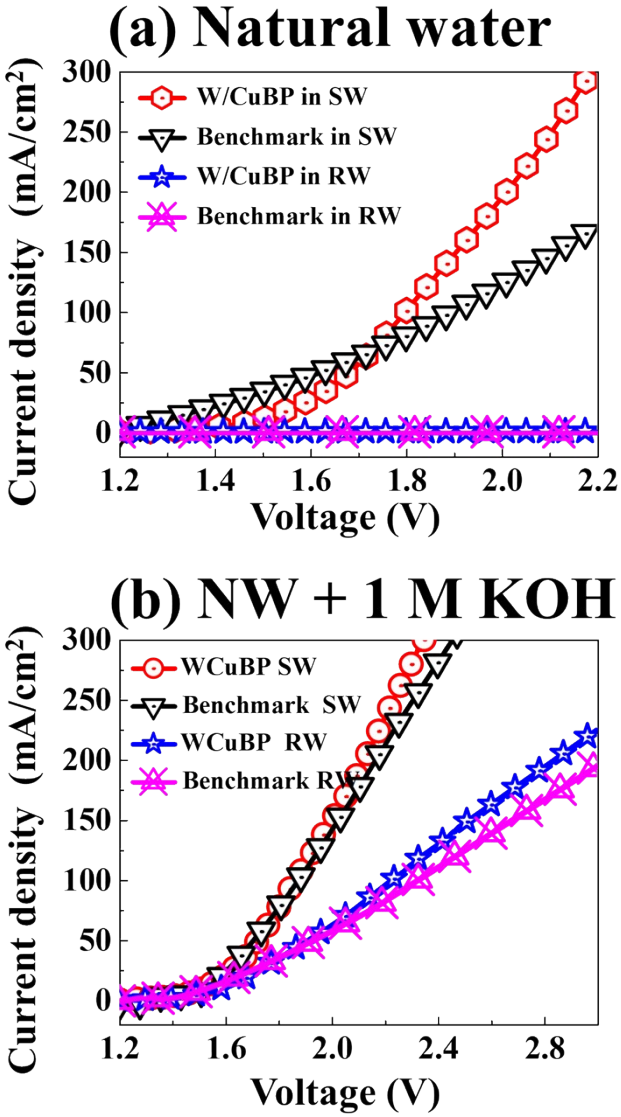

Figure S27. 2-E performance of WCuBP and benchmark Pt/C || RuO_2 in natural water. (a) Natural seawater and river water. (b) Natural water + 1 M KOH.

S-4. Post stability characterizations of WCuBP

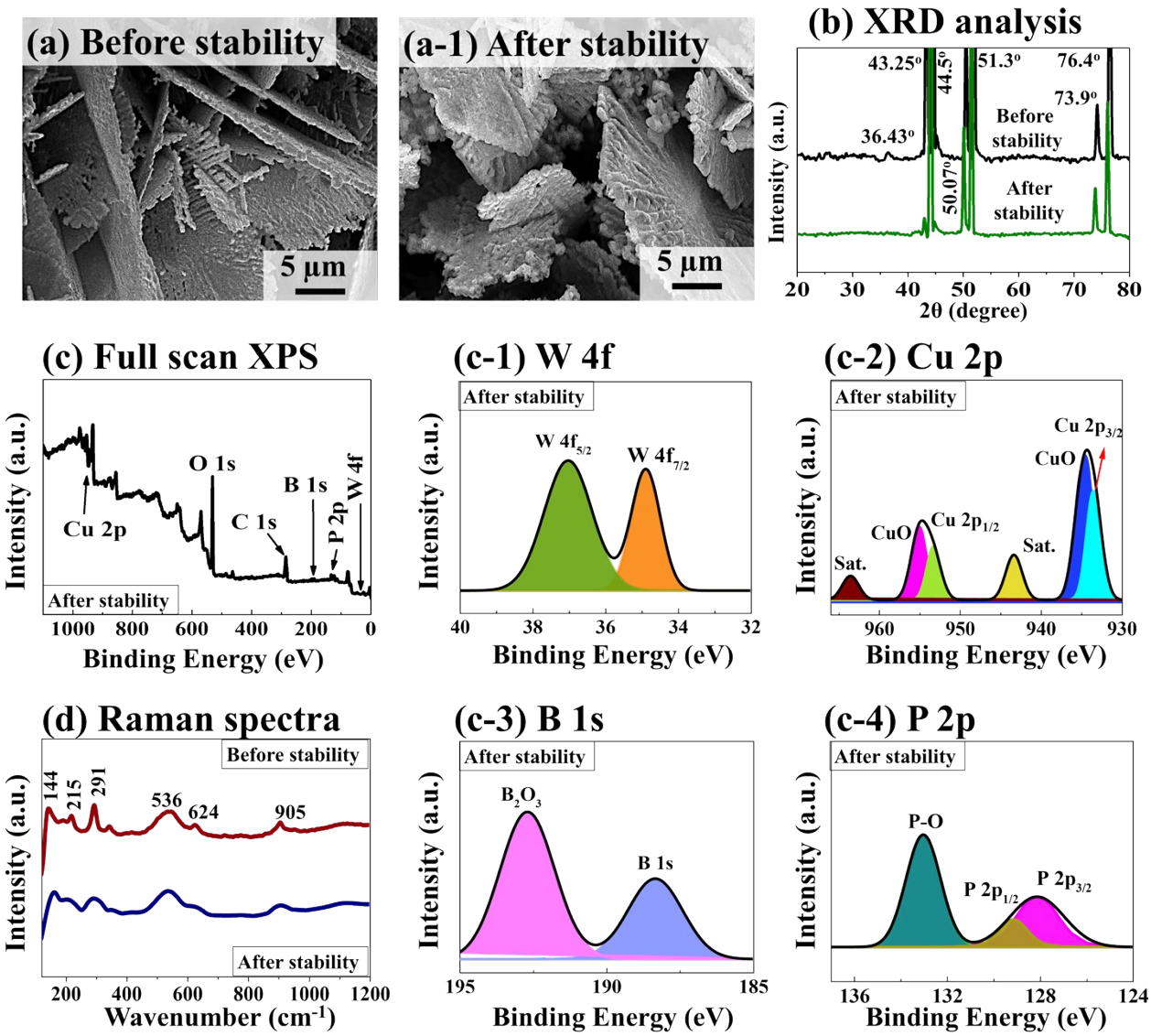

Figure S28: After stability analysis of the optimal WCuBP electrode. (a) – (a-1) Before/after stability SEM images. (b) XRD analysis before and after the stability test. (c) Full scan XPS spectra of the WCuBP electrode after the stability test. (c-1) – (c-4) High-resolution XPS spectra of the WCuBP electrode after stability. (d) Before/after stability Raman analysis.

References

1 S. Lin, R. Mandavkar, M. A. Habib, M. H. Joni, S. A. Dristy, S. Burse and J. Lee, *Adv. Sustain. Syst.*, 2025, **9**, 2400645.

2 N. Girija, S. S. Kuttan, B. N. Nair and U. N. S. Hareesh, *Results Eng.*, 2022, 100536.

3 S. Burse, R. Kulkarni, R. Mandavkar, M. A. Habib, S. Lin, Y.-U. Chung, J.-H. Jeong and J. Lee, *Nanomaterials*, 2022, **12**, 3283.

4 J. Gautam, S.-Y. Lee and S.-J. Park, *Adv. Compos. Hybrid Mater.*, 2024, **7**, 1–15.

5 M. H. Joni, S. Lin, M. A. Habib, S. A. Dristy, R. Mandavkar and J. Lee, *Nano Mater. Sci.*, DOI:https://doi.org/10.1016/j.nanoms.2024.12.009.

6 N. Elgrishi, K. J. Rountree, B. D. McCarthy, E. S. Rountree, T. T. Eisenhart and J. L. Dempsey, *J. Chem. Educ.*, 2018, **95**, 197–206.

7 S. Anantharaj and S. Noda, *Energy Adv.*, 2022, **1**, 511–523.

8 A. Ali, S. Muqaddas, H. Aldosari, S. Rashid, A. Hafiz, M. U. Saeed, A. Ahmad and M. Ahmad, *Carbon N. Y.*, 2024, **218**, 118709.

9 S. Anantharaj, S. R. Ede, K. Karthick, S. Sam Sankar, K. Sangeetha, P. E. Karthik and S. Kundu, *Energy Environ. Sci.*, 2018, **11**, 744–771.

10 N. Rasool, A. S. Alqarni, K. Ahmad, A. G. Al-Sehemi, A. M. A. Henaish and S. Aman, *Int. J. Hydrogen Energy*, 2024, **81**, 562–572.

11 T. Kim, S. B. Roy, S. Moon, S. Yoo, H. Choi, V. G. Parale, Y. Kim, J. Lee, S. C. Jun, K. Kang, S.-H. Chun, K. Kanamori and H.-H. Park, *ACS Nano*, 2022, **16**, 1625–1638.

12 S. Sultan, M. Ha, D. Y. Kim, J. N. Tiwari, C. W. Myung, A. Meena, T. J. Shin, K. H. Chae and K. S. Kim, *Nat. Commun.*, 2019, **10**, 1–9.

13 S. Lin, R. Mandavkar, M. A. Habib, M. H. Joni, S. A. Dristy, J.-H. Jeong and J. Lee, *Mater. Today Energy*, 2024, **46**, 101737.

14 L.-L. Xing, K.-J. Huang and L.-X. Fang, *Dalt. Trans.*, 2016, **45**, 17439–17446.

15 A. Rajput, A. Kundu and B. Chakraborty, *ChemElectroChem*, 2021, **8**, 1698–1722.

16 M. A. Habib, S. A. Dristy, S. Lin, M. H. Joni, M. Najibullah, R. Mandavkar and J. Lee, *Adv. Mater. Technol.*, 2025, **n/a**, 70021.

17 K. Ngamchuea, *Curr. Opin. Electrochem.*, 2023, **37**, 101193.

18 S. J. Raaijman, N. Arulmozhi, A. H. M. da Silva and M. T. M. Koper, *J. Electrochem. Soc.*, 2021, **168**, 96510.

19 A. Tiwari, H. H. Heenen, A. S. Bjørnlund, T. Maagaard, E. Cho, I. Chorkendorff, H. H. Kristoffersen, K. Chan and S. Horch, *J. Phys. Chem. Lett.*, 2020, **11**, 1450–1455.

20 A. Bagger, R. M. Arán-Ais, J. Halldin Stenlid, E. Campos dos Santos, L. Arnarson, K. Degn Jensen, M. Escudero-Escribano, B. Roldan Cuenya and J. Rossmeisl, *ChemPhysChem*, 2019, **20**, 3096–3105.

21 A. K. Engstfeld, T. Maagaard, S. Horch, I. Chorkendorff and I. E. L. Stephens, *Chem. Eur. J.*, 2018, **24**, 17743–17755.

22 S. A. Dristy, S. Lin, M. A. Habib, M. H. Joni, R. Mandavkar and J. Lee, *Int. J. Hydrogen Energy*, 2024, **96**, 321–332.

23 Y. Wang, X. Li, M. Zhang, J. Zhang, Z. Chen, X. Zheng, Z. Tian, N. Zhao, X. Han, K. Zaghib, Y. Wang, Y. Deng and W. Hu, *Adv. Mater.*, 2022, **34**, 1–10.

24 B. Xu, J. Liang, X. Sun and X. Xiong, *Green Chem.*, 2023, **25**, 3767–3790.

25 S. Anantharaj and S. Noda, *ChemElectroChem*, 2020, **7**, 2297–2308.

26 Z. Zhou, L. Wei, Y. Wang, H. E. Karahan, Z. Chen, Y. Lei, X. Chen, S. Zhai, X. Liao and Y. Chen, *J. Mater. Chem. A*, 2017, **5**, 20390–20397.

27 C. Chen, Y. Tuo, Q. Lu, H. Lu, S. Zhang, Y. Zhou, J. Zhang, Z. Liu, Z. Kang, X. Feng and D. Chen, *Appl. Catal. B Environ.*, 2021, **287**, 119953.